Ph.D. thesis

Studies of Electronic Properties in Atomically Thin Superconducting Films Modulated by Surface Acoustic Waves

Department of Physics, Graduate School of Science,
Osaka University

Masahiko Yokoi

2020

Contents

Preface

Negative differential resistances in semiconductors are well-established in tunnel diodes (or Esaki diodes) [1] and Gunn diodes [2], which are used in electronic oscillators and amplifiers, particularly at microwave frequencies. In those cases, the negative differential resistances are realized at finite bias regions. In other words, the absolute value of resistance, that is a voltage V divided by an applied current I, remains positive. In general, a negative resistance state at the zero bias limit violates either the conservation law of energy or the second law of thermodynamics, and thus is unstable in normal electric circuits [3]. By injecting an additional power from the outside, however, electronic transport properties can dramatically be changed. A typical example is microwave-induced zero resistance in a two-dimensional electron system (2DES) [4–6]. This nonequilibrium phenomenon occurs when the microwave frequency coincides with the Landau level splitting energy in the 2DES in a perpendicular magnetic field. In that case, however, the resistance does not take a negative value because the negative resistance state is energetically unstable in normal conductors where Ohm's law governs [3, 7].

In a superconducting state where the resistance is zero up to the critical current, Ohm's law is not valid anymore but the London equation is used to explain the electrodynamic properties [8]. When microwaves are irradiated to supercon-

ducting junctions, voltage jumps can be observed in the *I*-*V* curve [8], that is known as the *ac* Josephson effect. In this case, the resistance is still zero (or slightly positive). Here we consider the situation that atomically thin superconducting materials [9–14] on a piezoelectric substrate are irradiated by surface acoustic waves (SAWs). The SAW (more precisely Rayleigh wave) is an elastic wave traveling along the surface of piezoelectric substrate and is generated by applying an *ac* voltage to comb-shaped electrodes. The excited SAW can be coupled with the lattice system of 2D materials on the substrate, resulting in the modulation of electronic properties of the 2D materials [15, 16].

In this thesis, we demonstrate that the irradiation of SAWs induces a negative resistance at zero bias current limit, i.e., an opposite voltage drop with respect to the current direction, in a superconducting gap of atomically thin 2H-$NbSe_2$ films. Furthermore, the control experiments reveal that the negative resistance is caused by cooperative interplay between the charge density wave (CDW) modulated by the SAW and the superconductivity. To understand this observation, Chapter 1 gives the basics of superconductivity, CDW and SAW. Chapter 2 is devoted to some experimental details such as the sample fabrication and the setup. The experimental results are shown in Chapter 3. These experimental results are theoretically described in Chapter 4. Chapter 3 and 4 is based on my paper published in Science Advances [17]. In Chapter 5, we summarize this thesis.

Chapter 1

Introduction

In this thesis, we present experimental studies on electrical transport properties in layered superconducting thin films exposed to surface acoustic waves. As layered superconducting thin films, we have used $NbSe_2$ and NbS_2. The former has the charge density wave (CDW) phase below 33.5 K and also shows the superconducting transition below 7.2 K, while the latter has no CDW phase and shows the transition below 6 K [18].

In this chapter, we briefly review the following topics: superconductivity in Sec. 1.1, CDW in Sec. 1.2, and surface acoustic waves (SAWs) in Sec. 1.3. These are essential topic to understand the main results of the present thesis.

1.1 Superconductivity

1.1.1 Background of superconductivity

When temperature approaches to zero Kelvin, what happens to resistance in a metal? Does it continuously decrease down to zero Ohm? Or does it diverge as the

temperature approaches zero Kelvin? This was a mystery in the beginning of 20th century. Heike Kamerlingh Onnes succeeded in liquefying ^{4}He gas and measured the resistance of high purity mercury Hg down to $T = 4$ K, in order to give an answer to the above question. Unexpectedly, he found the superconductivity at $T = 4.2$ K [19, 20], which was coincidentally the boiling temperature of ^{4}He. Since then, the superconductivity has been extensively studied not only from the fundamental point of view but also from the applications side [8].

In 1957, J. Bardeen, L. N. Cooper and R. Schrieffer formulated the fundamental theory (BCS theory) which gives the microscopic descriptions of superconductivity [21]. BCS theory is based on an attractive interaction between two electrons at the Fermi surface via the electron-phonon interactions. Here, the electron pairs are assumed to have opposite signs in momentum space ($\boldsymbol{k}$ and $-\boldsymbol{k}$) and in spin space ($\sigma = \pm 1$). Due to the attractive interaction $-U < 0$, the electrons have a bound state, so called "Cooper pairs" [8]. This interaction term can be expressed by using the superposition of the creation and annihilation operators such as $c^\dagger_{\boldsymbol{k}\uparrow} c^\dagger_{-\boldsymbol{k}\downarrow}$ and $c_{-\boldsymbol{k}\downarrow} c_{\boldsymbol{k}\uparrow}$. In this situation, the ground state is no longer an eigenstate of the number of the electrons: $n^\dagger_{\boldsymbol{k}\sigma} = c^\dagger_{\boldsymbol{k}\sigma} c_{\boldsymbol{k}\sigma}$. Using a new operator $b^\dagger_{\boldsymbol{k}} = c^\dagger_{\boldsymbol{k}\uparrow} c^\dagger_{-\boldsymbol{k}\downarrow}$, the ground state can be described as follows: $|\Phi_{\mathrm{G}}\rangle = \prod_{\boldsymbol{k}=\boldsymbol{k}_1,\ldots,\boldsymbol{k}_M} (u_{\boldsymbol{k}} + v_{\boldsymbol{k}} b^\dagger_{\boldsymbol{k}})|0\rangle$, where the ket vector $|0\rangle$ denotes the vacuum state and $|u_{\boldsymbol{k}}|^2 + |v_{\boldsymbol{k}}|^2 = 1$. The operator $b^\dagger_{\boldsymbol{k}}$ creates the two electrons, namely the Cooper pair, and the superconducting ground state is described as a superposition of the Fock states of Cooper pairs. The excited state can be described by a quasiparticle excitation. The excitation energy is given by $E_{\boldsymbol{k}} = (\xi^2_{\boldsymbol{k}} + |\Delta_{\boldsymbol{k}}|^2)^{1/2}$, where $\xi_{\boldsymbol{k}}$ is the dispersion relation in the metal state, and Δ denotes the energy gap to excite the quasiparticle, i.e.,

$\Delta = -U \sum_{\boldsymbol{k}} \langle b_{\boldsymbol{k}} \rangle$.

On the other hand, V. L. Ginzburg and L. D. Landou (GL) developed the phenomenological theory of superconductivity based on Landou theory which explains a general phase transition in 1950 [22]. As verified by L. P. Gor'kov, Ginzburg-Landou (GL) theory can be derived from the BCS Hamiltonian [23,24].

1.1.2 Electrical conduction of superconductivity

The most remarkable property of the superconductor may be zero resistance. According to GL theory, the free energy f per unit volume can be described as follows [8]:

$$f = f_n + \alpha|\phi|^2 + \frac{\beta}{2}|\phi|^4 + \frac{1}{2m^*}\left|(\frac{\hbar}{i}\boldsymbol{\nabla} - \frac{e^*}{c}\boldsymbol{A})\phi\right|^2 + \frac{h^2}{8\pi}, \tag{1.1}$$

where ϕ is the superconducting order parameter, $\boldsymbol{A}$ is the vector potential, and h is the applied magnetic field. The first term f_{n} is the free energy of the normal state and the last term corresponds to the magnetic energy. The prefactor β should be positive for the stability of the system. The parameter $\alpha \propto T - T_{\mathrm{C}}$ describes the phase transition: for $\alpha > 0$ ($T > T_{\mathrm{C}}$), the free energy has a minimum at $\phi = 0$, while $\alpha < 0$ ($T < T_{\mathrm{C}}$), the free energy has a minimum at a finite ϕ value.

The free energy (Eq. (1.1)) contains two variables: the order parameter and the vector potential. In order to obtain the equation of the supercurrent, we have to perform the variation method over the vector potential $\boldsymbol{A}$. This leads to the

following simple relation between the supercurrent and the vector potential:

$$\begin{aligned} \boldsymbol{J}_{\mathrm{SC}}(\boldsymbol{r}) &= \frac{c}{4\pi}\boldsymbol{\nabla}\times\boldsymbol{h} \\ &= \frac{e^*\hbar}{2im^*}(\phi^*\boldsymbol{\nabla}\phi-\phi\boldsymbol{\nabla}\phi^*)-\frac{e^{*2}}{m^*c}|\phi|^2\boldsymbol{A}. \end{aligned} \tag{1.2}$$

The first and second terms show the phase current originating from the inhomogeneous order parameter. The last term shows the supercurrent driven by the vector potential $\boldsymbol{A}$.

For a homogeneous system, the order parameter does not depend on the position. Thus, Eq. (1.2) can be simplified as:

$$\frac{4\pi}{c}\boldsymbol{J}_{\mathrm{SC}} = -\lambda^{-2}\boldsymbol{A}, \tag{1.3}$$

$$\lambda^{-2} = \frac{4\pi e^{*2}}{m^*c^2}|\phi|^2. \tag{1.4}$$

This relation is consistent with the description suggested by F. London and H. London, namely London equation [25]. The value λ is the penetration depth of magnetic field in a superconductor. London equation implies that the supercurrent is essentially inductive. When the electrostatic potential is zero, the electric field is expressed using the vector potential: $\boldsymbol{E}=-\frac{\partial\boldsymbol{A}}{\partial t}$. By taking a time derivative of Eq. (1.3), the time development of the supercurrent induces the electric field, or voltage: $\boldsymbol{E}\propto-\frac{\partial\boldsymbol{J}_{\mathrm{SC}}}{\partial t}$. Indeed, the resistance (or impedance) is zero when the supercurrent has only the *dc* component, while the resistance takes a non-zero value when the supercurrent has an *ac* component [26].

By increasing the current, the superconducting state is broken at the critical

current I_C. The critical current can easily be calculated for a superconducting thin film which is thinner than the coherence length. This guarantees the homogeneous superconducting system. Assuming a finite supercurrent velocity $\boldsymbol{v}_{SC} = \frac{1}{m}(\boldsymbol{p}_{SC} - \frac{e^*}{c}\boldsymbol{A}) = \frac{1}{m}(\hbar\boldsymbol{\nabla}\varphi - \frac{e^*}{c}\boldsymbol{A})$, the free energy Eq. (1.1) takes a minimum value when the following relation is fulfilled: $\boldsymbol{J}_{SC} = e^*\phi_\infty^2(1 - \frac{m^* v_{SC}^2}{2|\alpha|})\boldsymbol{v}_{SC}$, where $\phi_\infty = -\alpha/\beta$. The critical current density can be obtained when $|\boldsymbol{J}_{SC}|$ takes a maximum value as a function of the supercurrent velocity:

$$J_C = e^*\phi_\infty^2 \frac{2}{3}\sqrt{\frac{2\alpha}{3m^*}}. \tag{1.5}$$

1.1.3 Josephson junction

In Chap. 4, we will analyze our experimental results by using the Josephson junction (JJ) model [8]. A JJ consists of two superconducting electrodes coupled by a weak link, which is an insulating barrier, a thin metallic layer, or a physical constriction. For simplicity, we consider the case that the two superconducting electrodes are made of the same material via the weak link. In such a situation, the amplitude of the superconducting gap has the same value, but the phase of the order parameter can take different values, as illustrated in Fig. 1.1.1(a). In 1962, Josephson theoretically showed that a supercurrent can penetrate through the weak link into the other electrode without a voltage drop [27]. The fundamental description of the supercurrent at the JJ can be obtained from the GL theory [8], but practically, the electrical properties of the JJ depend on the detailed geometries and superconducting materials, which results in the complicated theoretical description of the JJ [28].

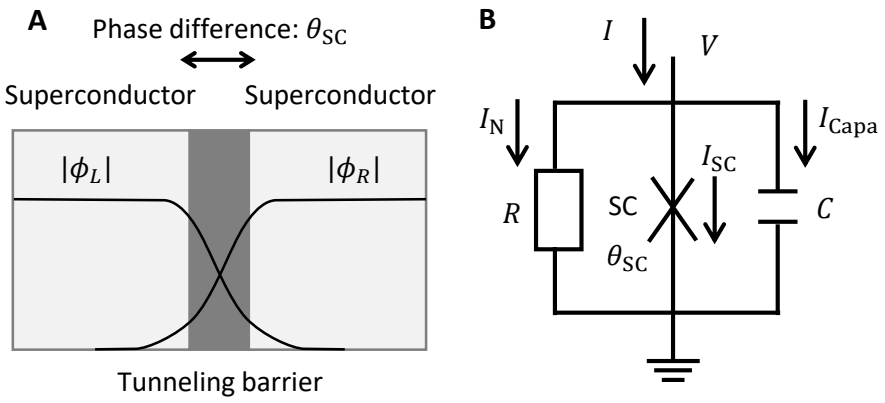

Figure 1.1.1: (A) Schematic image of JJ. (B) Equivalent circuit of the RCSJ model.

One of the most successful models about the JJ is the resistively and capacitively shunted junction (RCSJ) model [8]. This model is valid when the phase difference at the junction is homogeneous. In this model, there are three current paths in parallel, i.e., a supercurrent, a normal current, and a capacitance (see Fig. 1.1.1). The supercurrent can be described as $I_{SC} = I_C \sin\theta_{SC}$, where θ_{SC} denotes the phase difference between the two superconducting electrodes. The voltage drop induced by the supercurrent pass can be expressed as the time derivative of the phase: $V = \frac{\hbar}{2e}\frac{d\theta_{SC}}{dt}$. The resistance in the normal state R is adopted for the normal current pass. According to Kirchhoff's circuit laws, the total current can be described as follows:

$$
\begin{aligned}
I &= I_{SC} + I_R + I_{Capa} && (1.6)\\
&= I_C \sin\theta_{SC} + V/R + C\frac{dV}{dt} && (1.7)\\
&= I_C \sin\theta_{SC} + \frac{1}{R}\frac{\hbar}{2e}\frac{d\theta_{SC}}{dt} + C\frac{\hbar}{2e}\frac{d^2\theta_{SC}}{dt^2}, && (1.8)
\end{aligned}
$$

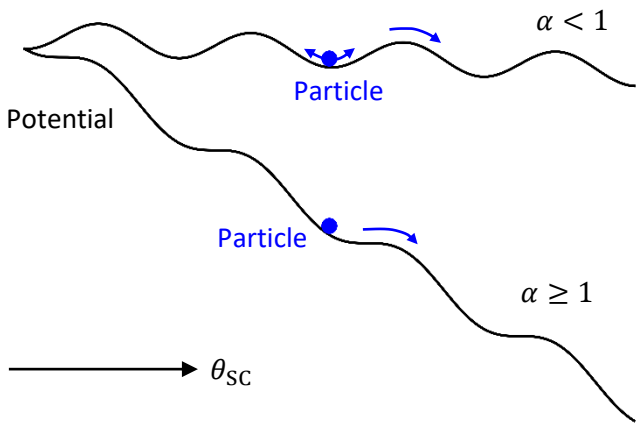

Figure 1.1.2: Schematic image of the washboard model. The particle (blue dot) moves the tilted sinusoidal potential.

where C denotes the capacitance and the notation of each current path is shown in Fig. 1.1.1. By introducing the dimensionless quantities $\tau = \omega_J t$ and $\beta = 1/\omega_J RC$, where $\omega_J = \sqrt{2eI_C/\hbar C}$, Eq. (1.6) can be simplified as follows:

$$\frac{d^2\theta_{SC}}{d\tau^2} + \beta\frac{d\theta_{SC}}{d\tau} + \sin\theta_{SC} = \alpha, \tag{1.9}$$

where $\alpha = I/I_C$ denotes the normalized current. It should be noted that Eq. (1.9) is a nonlinear differential equation, and thus we cannot obtain its analytical solution. However, by using the analogy for the washboard model (see Fig. 1.1.2), one can capture the essential point of the RCSJ model. The washboard model is based on the motion of a particle in the tilted sinusoidal potential. The position of the particle shows the phase difference θ_{SC} in the JJ. On the left hand side of Eq. (1.9), the second term describes the dumping and the third term corresponds to the periodical potential. The constant $\alpha = I/I_C$ corresponds to the gradient of the potential.

Let us first consider the situation when I increases from zero to I_C, i.e., $\alpha > 1$. In this case, the particle is confined by the sinusoidal potential and then is relaxed into a minimum of the potential. Because the time derivative of θ_{SC} is proportional to the voltage, the induced voltage is zero by taking the time average. When the current exceeds the critical current ($|\alpha| \geq 1$), there is no minimum in the potential. Thus, the particle slips down the slope of the potential and a finite voltage is induced.

When I decreases from I_C to zero, the hysteresis appears below I_C. This is because the particle has a large kinetic energy which exceeds the sinusoidal potential. Therefore, even though I becomes smaller than I_C, the particle continues to go down the potential, and the voltage drop does not disappear. By decreasing I more, the particle can be trapped when the damping exceeds the acceleration by the tilt. Then, the particle is confined in a minimum of the potential and the JJ shows the zero voltage.

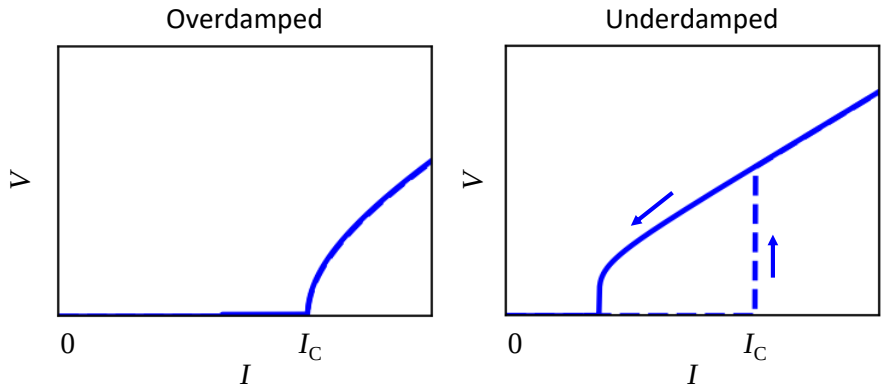

Figure 1.1.3: I-V cures of the JJ in the overdamped case $\beta_J \gg 1$ (left) and in the underdamped case $\beta_J < 1$ (right).

The current-voltage properties (I-V curves) of the JJ are shown in Fig. 1.1.3. When the capacitance C is small and the damping term dominates Eq. (1.9) (overdamped, $\beta \gg 1$), the kinetic energy of the particle is dissipated and the hysteresis does not appear (see the left graph of Fig. 1.1.3). In this case, $V = 0$ up to $\alpha = 1$ and $V = RI\sqrt{(I/I_C)^2 - 1}$ for $\alpha \geq 1$. When the damping is not strong (underdamping, $\beta < 1$), the hysteresis can be observed (see the right graph of Fig. 1.1.3).

It is also known that the RCSJ model describes well the dynamics of JJ even in the high frequency regime [8,28]. That is another reason why we have adopted the model in the present thesis. As will be detailed later on, we have observed the I-V curves, which can be described by a typical overdamped JJ, in the superconducting thin films 3.2. We thus discuss the experimental results based on the RCSJ model in Chap. 4.3.

1.2 Charge densiy wave (CDW)

1.2.1 Background of CDW

It was first pointed out by Peierls that a one-dimensional metal coupled to the underlying lattice is not stable at low temperatures [29]. The ground state is characterized by a collective mode formed by electron-hole pairs involving the wave vector $q = 2k_{\mathrm{F}}$ (k_{F}: Fermi wave number). This state is called the CDW. In 1954, Fröhlich proposed that the CDW would carry an electric current without any dissipation, which could lead to the superconductivity [30]. However, later experiments have revealed that the CDW cannot move freely due to the pinning by the commensuration with the lattice or some impurities in the crystal.

The CDW materials have been intensively investigated since 1970s. The dynamics of the CDW was first observed by Fogle and Perlstein in 1972 [31]. They observed a nonlinear electrical conduction at low electric fields in the blue bronze $K_{0.30}MoO_3$ below a metal-insulator transition. By now, the dynamics of the CDW is well studied in a broad range of low dimensional materials, such as the traditional dichalcogenides [32], the traditional trichalcogenides [33, 34], and the organic compounds [35, 36].

In a low dimensional electronic system, the electron-phonon interactions on the Fermi surface are drastically enhanced due to the singularity of the response function caused by the Fermi surface nesting. The electron-phonon interactions reduce the energy of the phonon mode at the wave number of $k = \pm 2k_{\mathrm{F}}$, which induces the static lattice strains (phonon softening, see Fig. 1.2.1). Since the lattice strains and electronic carriers strongly interact each other, they should be

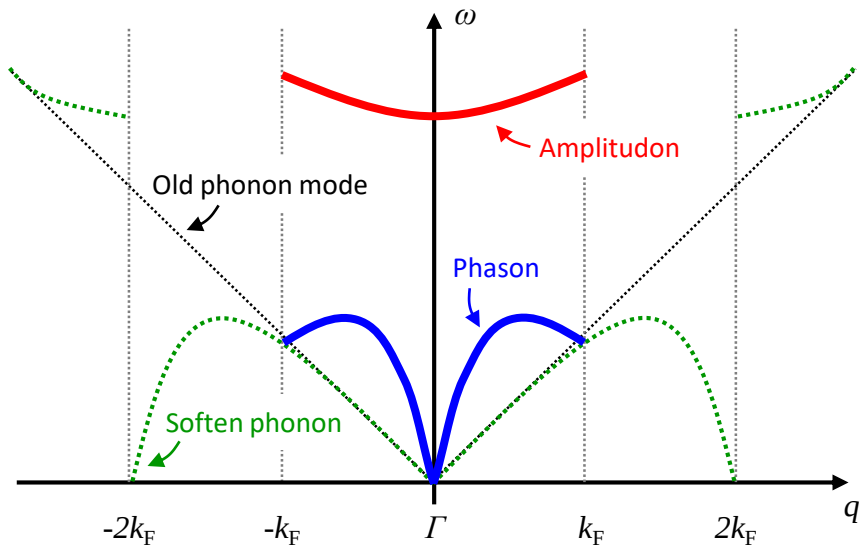

Figure 1.2.1: Dispersion relation of a amplitudon and a phason.

treated as the combined waves which are defined as charge density waves (CDWs). The charge density distribution and the lattice distortion have the same periodicity as $\lambda_{\mathrm{CDW}} = 2\pi/2k_{\mathrm{F}}$. Since these amplitudes are proportional to each other, the charge density distribution or the lattice distortion can be selected as the order parameter [37].

Depending on the commensurability of the modulation in the charge density with the underlying lattice, the CDW states are classified into two types, a commensurate CDW (CCDW) state and an incommensurate CDW (ICDW) state. The CDW states are defined as the CCDW when the ratio of the CDW wavelength $\lambda_{\mathrm{CDW}} = 2\pi/2k_{\mathrm{F}}$ to the lattice constant a is a rational number. As we will describe below, the lattice gives the spatially periodic potential to the CCDWs, which pin the CDW motion. In the case of the ICDW state, when a ratio λ_{CDW}/a is an irrational number, the pinning does not seems to emerge intuitively because the

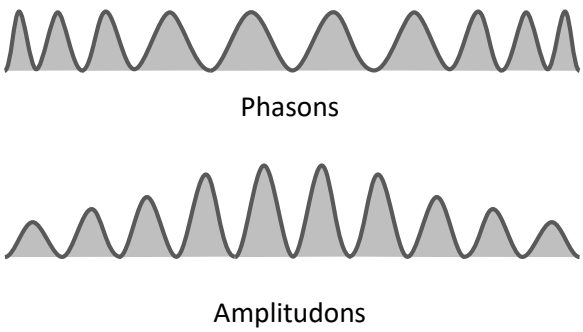

Figure 1.2.2: Schematic images of phasons (top) and amplitudons (bottom).

potential energy given by the lattice is invariant to the translational motion. Practically, however, ICDWs are also pinned by the potential of the impurities. In this section, we will describe the dynamics of the CDWs without the pinning in Sec. 1.2.2 and with the pinning in Sec. 1.2.3.

1.2.2 Dynamics of CDW without pinning

Let us consider the case without the pinning for simplicity. The ground state of the CDW has a unique order parameter, which is spatially homogeneous. There are two types of the excited states, i.e., individual and collective excitations. The individual excitation is a single electron excitation beyond the Peierls gap energy (typically $\sim$ 100 meV). On the other hand, the collective excitation is described as a spatial and temporal modification of the order parameter. The modulations of the order parameter in the amplitude and in the phase are called "amplitudons" and "phasons", respectively (Fig. 1.2.2). Due to the electron-phonon interactions, the collective excitations are induced not only by the lattice strain but also by the modulation in the carrier densities.

The softening of phonon opens the phonon band gap at $k = \pm 2k_{\mathrm{F}}$, leading to the two branches as shown in Fig. 1.2.1. The spatial periodicity minimizes the Brillouin zone $|k| \leq k_{\mathrm{F}}$, in which the phonon branches are folded. As a result, the softened phonon modes and the old phonon mode at the Γ point are degenerate each other. The branches around the Γ point corresponds to the collective excitations in the CDWs; the zero gap mode and the finite gap mode correspond to the phason and the amplitudon, respectively. Lee-Rice-Anderson theoretically introduced the dispersion relation as follows [38]:

$$\begin{cases} {\omega_+}^2(q) = \lambda {\omega_0}^2(2k_{\mathrm{F}}) + \frac{m}{3m^*} v_{\mathrm{F}}^2 q^2 & (\text{Amplitudons}) \\ {\omega_-}^2(q) = \frac{m}{m^*} v_{\mathrm{F}}^2 q^2 & (\text{Phasons}), \end{cases} \tag{1.10}$$

where ω_0, v_{F} and λ are the angular frequency of the phonon in the normal state, the Fermi velocity, and the dimensionless electoron-phonon interaction, respectively. The effective mass m^* of the electron in the CDW state is given by $m^*/m = 1 + (2|\Delta|)^2/\lambda\hbar^2\omega_0(2k_{\mathrm{F}})^2$, where m is the effective band mass. The effective mass of the electron in the CDW state is enhanced by phonon because of the electron-phonon interactions.

The charge density ρ in the isolated one-dimensional CDW with the nesting vector Q is described as

$$\rho(x) = \rho_0 + \rho_1 \cos(Qx + \phi_{\mathrm{CDW}}), \tag{1.11}$$

where $Q = 2k_{\mathrm{F}}$, $\rho_0 = -en_{\mathrm{e}}$ (n_{e} is the carrier density). ρ_1 and ϕ_{CDW} are the amplitude and the phase of the CDW, respectively. The charge density modulation $\Delta\rho$

and the current j_{CDW} caused by the CDW motions can be described by using the spatial and the temporal derivatives of $\phi_{\mathrm{CDW}}(x,\, t)$, respectively:

$$\Delta\rho = +\frac{e}{\pi}\frac{\partial\phi_{\mathrm{CDW}}}{\partial x} \tag{1.12}$$

$$j_{\mathrm{CDW}} = n_{\mathrm{e}} e v_{\mathrm{d}} = -\frac{e}{\pi}\frac{\partial\phi_{\mathrm{CDW}}}{\partial t}. \tag{1.13}$$

Here, v_{d} is the drift velocity of the CDW.

When there is no pinning potential, a total energy of the CDW state can be described by taking the summation of the kinetic energy E_{k} and the elastic energy E_{u}. Using the effective velosity $\bar{v} \equiv {v_{\mathrm{ph}}}^2/v_{\mathrm{F}} = m v_{\mathrm{F}}/m^*$ (v_{ph} is the phason velosity), E_{k} can be written as

$$E_{\mathrm{k}} = \frac{1}{2} n_{\mathrm{e}} m^* v_{\mathrm{d}}^2 = \frac{\hbar}{4\pi\bar{v}}\dot{\phi}_{\mathrm{CDW}}^2. \tag{1.14}$$

Because the elastic constant c can be described as $c = (\frac{\hbar}{2\pi\bar{v}}){v_{\mathrm{ph}}}^2$, E_{u} is derived as

$$E_{\mathrm{u}} = \frac{c}{2}|\nabla\phi_{\mathrm{CDW}}|^2 = \frac{\hbar {v_{\mathrm{ph}}}^2}{4\pi\bar{v}}|\nabla\phi_{\mathrm{CDW}}|^2. \tag{1.15}$$

Thus, the Lagrangian of the CDW is expressed as:

$$\mathscr{L} = \int dx\{E_{\mathrm{k}} - E_{\mathrm{u}} - E_{\mathrm{es}}\} \tag{1.16}$$

$$= \frac{\hbar}{4\pi\bar{v}}\int dx\left\{\dot{\phi}_{\mathrm{CDW}}^2 - {v_{\mathrm{ph}}}^2|\nabla\phi_{\mathrm{CDW}}|^2 + \frac{4\bar{v}eE_{\mathrm{ex}}x}{\hbar}\nabla\phi_{\mathrm{CDW}}\right\}, \tag{1.17}$$

where the last term $E_{\mathrm{es}} = -\frac{eE_{\mathrm{ex}}x}{\pi}\nabla\phi_{\mathrm{CDW}}$ corresponds to the potential energy by the external electric field. The Lagrange equation gives the equation of the CDW

motion under the electric field E_{ex}:

$$\frac{\partial^2 \phi_{\mathrm{CDW}}}{\partial t^2} - {v_{\mathrm{ph}}}^2 \frac{\partial^2 \phi_{\mathrm{CDW}}}{\partial x^2} = -\frac{\pi n_e e}{m^*} E_{\mathrm{ex}}. \tag{1.18}$$

Equation (1.18) is a second-order linear partial differential (hereafter wave equation) equation accelerated by the electric field E. The coefficient n_e/m^* for the accelerated term implies that all of the condensed electrons are collectively accelerated and contribute to drive the CDW motion. When there is no pinning potential, the dynamics of CDW can be described by Eq. (1.18).

1.2.3 Dynamics of CDW with pinning

In a real CDW material, the pinning due to the lattice commensuration or the defect strongly affects to the CDW motions. Here, we adopt the sine-Gordon model to describe the pinning potential. In the case of the lattice commensuration, the sinusoidal pinning potential depends on the degeneracy M of the ground states. The effect of the inhomogeneous defects can be reflected by introducing the randomness into the pinning potential [39, 40]. Thus, the pinning potential is expressed as the spatially periodic potential $E_{\mathrm{p}} = -\frac{\hbar}{4\pi\bar{v}} \frac{{\omega_F}^2}{M^2} \cos M\phi_{\mathrm{CDW}}$ in the Lagrangian, where ω_F is a coefficient with the dimension of angular frequency. Then, the wave equation (1.18) can be rewritten as:

$$\frac{\partial^2 \phi_{\mathrm{CDW}}}{\partial t^2} - {v_{\mathrm{ph}}}^2 \frac{\partial^2 \phi_{\mathrm{CDW}}}{\partial x^2} + \frac{{\omega_F}^2}{2M} \sin M\phi_{\mathrm{CDW}} = -\frac{\pi n_e e}{m^*} E_{\mathrm{ex}}. \tag{1.19}$$

The zero electric field limit ($E_{\rm ex} = 0$) in Eq. (1.19) corresponds to the well-known sine-Gordon equation. Due to the periodical potential, the energy gap is induced in the dispersion relation of the phason:

$$\omega_-{}^2(q) = v_{\rm ph}^2 q^2 + \frac{\omega_F{}^2}{M}. \tag{1.20}$$

If the phase of the CDW is homogeneous, the second term of Eq. (1.19) can be ignored. Assuming an additional damping term $\gamma\frac{\partial\phi_{\rm CDW}}{\partial t}$, Eq. (1.19) can be rewritten as:

$$\frac{\partial^2\phi_{\rm CDW}}{\partial t^2} - \gamma\frac{\partial\phi_{\rm CDW}}{\partial t} + \frac{\omega_F{}^2}{M}\sin M\phi_{\rm CDW} = -\frac{\pi n_e e}{m^*}E_{\rm ex}. \tag{1.21}$$

This is the most convenient classical model to describe the dynamics of the CDW. Equation (1.21) is similar to the washboard model (RSCJ model) in the Josephson circuit (see Eq. (1.9)). In Eq. (1.21), the third term on the left hand side corresponds to the sinusoidal potential and the electric field tilts the sinusoidal potential (see Fig. 1.1.2). When the external electric field $E_{\rm ex}$ is smaller than the threshold value, the particle in Fig. 1.1.2 is confined to the sinusoidal potential and the CDW current does not flow. On the other hand, when $E_{\rm ex}$ exceeds the threshold value, the particle goes down the potential, and then the finite current is induced. This behavior, known as the CDW sliding, has been observed in many kinds of CDW materials [37]. This model gives us the qualitative description of the CDW sliding. In Sec. 4.2, we will make a discuss, based on the washboard model assuming the homogeneous CDW. However, it should be noted that several reports pointed out that the washboard model does not describe the transient

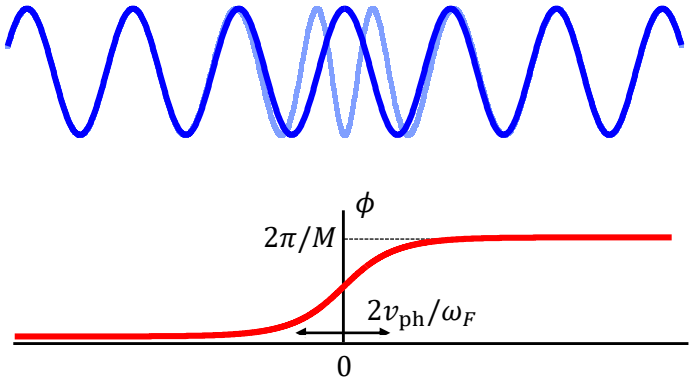

Figure 1.2.3: Schematic image of a soliton.

dynamics [41–43] and the high frequency response [44].

To describe high frequency dynamics, we have to treat Eq. (1.19) without assuming the homogeneity of the CDW phase. Because the sine-Gordon equation is nonlinear, it is difficult to obtain a general solution analytically. When $E_{\mathrm{ex}} = 0$, however, it is known that a particular solution of the sine-Gordon equation (Eq. (1.19)) can be obtained by considering Galilean transformation [37]. This particular solution is described as follows:

$$\phi^{\pm}_{\mathrm{CDW}}(x,\, t) = \frac{4}{M}\arctan\left[\exp\left\{\pm\frac{\omega_F}{\sqrt{v_{\mathrm{ph}}^2 - u^2}}(x - ut)\right\}\right], \tag{1.22}$$

where u is an arbitrary constant with the dimension of velocity. The schematic image of the soliton solution is shown in Fig. 1.2.3. Generally, the soliton in the sine-Gordon model has a topological charge [45] which is an effective charge normalized by M in the CDW soliton: $e^* = 2e/M$. Because of the conservation of the topological charge, however, the single soliton excitation is forbidden.

A soliton pair model was first proposed by Maki in 1977 [46]. According to this model, soliton-antisoliton pairs are nucleated. The pairs have opposite signs in e^*. However, this model does not explain the sharp threshold field in the I-V properties. To overcome this problem, Krive and Rozhavsky proposed to take into account the electrostatic energy caused by the charges of the induced soliton-antisoliton pairs [47]. The pair of the charges induces an internal electric field $\boldsymbol{E}^*$, and thus the electrostatic energy $\frac{1}{2}\varepsilon(\boldsymbol{E}_{\rm ex}+\boldsymbol{E}^*)^2$ prevents additional nucleation of the soliton-antisoliton pairs (Coulomb blockade). ε and $\boldsymbol{E}_{\rm ex}$ denote the permittivity and the external electric field. This model including the Coulomb blockade explains that in real experiments, the threshold field is much smaller than the classical wash board model [42, 48]. Furthermore, it was also reported that the pair excitation may be necessary to explain the dielectric response [34, 48]. These reports suggest that the pair excitation should be taken into account for understanding the dynamics of CDW precisely. In Sec. 4.3, we will make some discussions based on the soliton-antisoliton pair excitation.

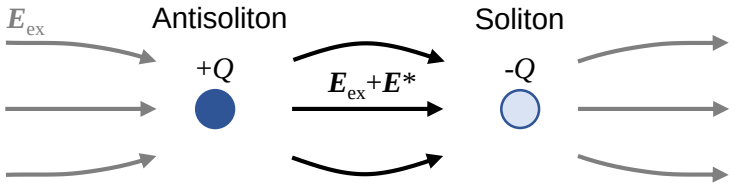

Figure 1.2.4: A schematic image of the soliton-antisoliton pair. The arrows represent the electric field.

1.3 Surface acoustic waves (SAWs)

1.3.1 Basics of SAWs

Surface acoustic waves (SAWs) can be generated at the free surface of an elastic solid [49,50]. This phenomenon has been exploited as an analog signal processing for several decades. Originally, Rayleigh reported the propagation of SAWs at the free surface of a homogeneous isotropic elastic solid in 1855 [51]. The concept of SAW plays an important part in seismology. Indeed, the presence of the SAWs in earthquake was verified using the seismograph recording techniques [52].

The potential for electronic device application was first suggested in 1965. White and Voltmer invented an interdigital transducer (IDT) to generate and detect SAWs on a piezoelectric surface [53]. The IDT consists of two pairs of comb-shaped electrodes deposited on the surface of a piezoelectric crystal such as quartz (see Fig. 1.3.1). It enabled us to design the versatile analog electrical filters operating at selected frequencies in the range from about 10 MHz to 1 GHz or above. By now, a wide variety of SAW devices have been developed, including delay lines, bandpass filters and resonators [49, 50].

The SAW, often called a Rayleigh wave, propagates along the plane surface of an isotropic solid half-space [54]. It consists of a compressional wave and a shear wave (sometimes two shear waves coupled together) in a fixed ratio. One component of this physical displacement is parallel to the SAW propagation axis, while the other is normal to the surface. The wave has a linear dispersion, with a smaller velocity than that of the bulk shear wave.

Figure 1.3.2 shows the instantaneous distortion of atoms, with much exagger-

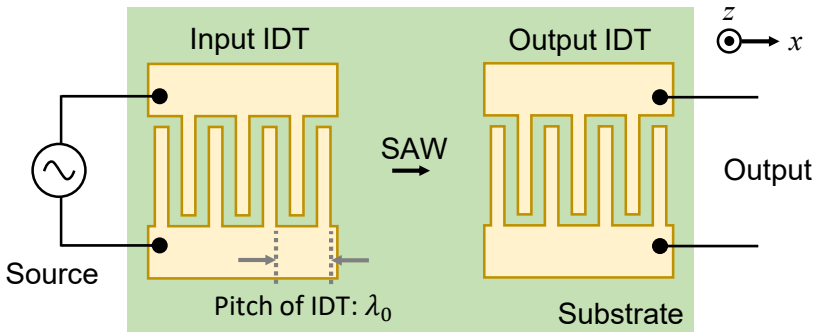

Figure 1.3.1: A schematic image of basic SAW device.

ated displacements [50]. The atoms describe an elliptical path. The propagation of a SAW on an unbounded elastic surface is associated mechanically with a time-dependent elliptical displacement of the surface structure. In principle, the SAW propagation in a piezoelectric medium could be expressed by combining the mechanical equation with the Maxwel's equations. However, since the mechanical wave is around 10^5 times slower than the velocity of light, the mechanical equation would dominate the combined wave equation. The induced electrical potential Φ at the surface of material can be described as a traveling wave of potential such as

$$\Phi = |\Phi| e^{i(\omega_{\mathrm{SAW}} t - k_{\mathrm{SAW}} x)} e^{-k_{\mathrm{SAW}}|z|}, \tag{1.23}$$

where $\omega_{\mathrm{SAW}} = 2\pi f_{\mathrm{SAW}}$ and $k_{\mathrm{SAW}} = 2\pi/\lambda_{\mathrm{SAW}}$ denote the angular frequency and wave number of SAW, respectively. There is the following relation between these values: $v_{\mathrm{SAW}} = f_{\mathrm{SAW}}\lambda_{\mathrm{SAW}}$. The first term $e^{i(\omega_{\mathrm{SAW}} t - k_{\mathrm{SAW}} x)}$ in Eq. (1.23) is related to the traveling wave distribution of potential along the SAW propagation axis at the surface. The second term $e^{-k_{\mathrm{SAW}}|z|}$ is related to the penetration of SAW from

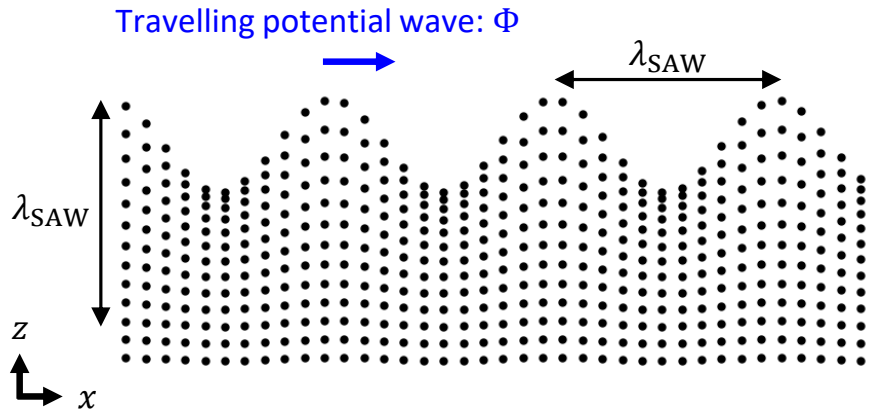

Figure 1.3.2: A schematic image of SAW during propagation. Dots represent the instantaneous distortion of the atoms, with much exaggerated displacements. The amplitude of SAW decays exponentially away from the surface. The blue arrow indicates the propagation direction of the SAW.

the surface into the bulk. The amplitude of SAW decays exponentially away from the surface, while the penetration depth is of the order of wavelength λ_{SAW}.

The piezoelectricity of the material enables us to generate SAWs electronically by using an IDT [49]. The transducer consists of two pairs of comb-shaped electrodes. Figure 1.3.1 shows a basic SAW device using two transducers. Here, one IDT is to generate and the other is to receive the SAW. When a *dc* voltage is applied to the two comb-shaped electrodes, the input IDT on the left induces a periodic electric field and the corresponding elastic strain because of the piezoelectric effect. By applying a *ac* voltage to the input IDT, each electrode generates the weak SAW. They are constructively superposed when the wavelength λ_{SAW} matches the pitch of the electrode λ_0, and then the strong SAW is generated. At the output, the other transducer receives the SAW in a reciprocal manner, by converting the SAW to an output voltage. The mathematical model is described in

Sec. 2.1. In commercial production, the minimum pitch is $\lambda_0 \sim 500$ nm, giving a maximum SAW frequency of about 5 GHz.

1.3.2 SAW devices in mesoscopic systems

In 1986, Wixforth *et al*. reported that electrons in a two dimensional electron gas system (2DES) confined in a GaAs/AlGaAs heterostructure interact with SAWs [55,56]. One can define the quantum system, such as the one-dimensional channel and the quantum dot, in the 2DES by the gate voltage [57]. The SAW modulates the electrical potential in the 2DES specially and temporally, and then the electrical conduction of the 2DES can be modulated. Such SAW techniques have given rise to a new field of the mesoscopic physics.

One of the intriguing issues is single electron transfer. When the SAW is irradiated to the one-dimensional channel, defined by the split gate in the 2DES, the 2D electron gas is conveyed one by one from one lead to the the other through the narrow channel. As a result, the current is quantized as $I = nef_{\mathrm{SAW}}$ [58], where f_{SAW} is the frequency of the SAW. This quantized current is considered to be a candidate of the current standard [59–61].

The single electron transfer technique has also attracted attentions in terms of quantum information [62]. The development of mesoscopic physics has enabled us to manipulate the quantum state of single electron with high precision. This is an important progress for quantum information. The SAW is expected to transfer single electron without breaking the quantum state. Hermelin *et al*. and McNeil *et al*. simultaneously reported single electron transfers using the SAWs in 2011 [63, 64]. In these experiments, an electron confined in the left quantum dot was

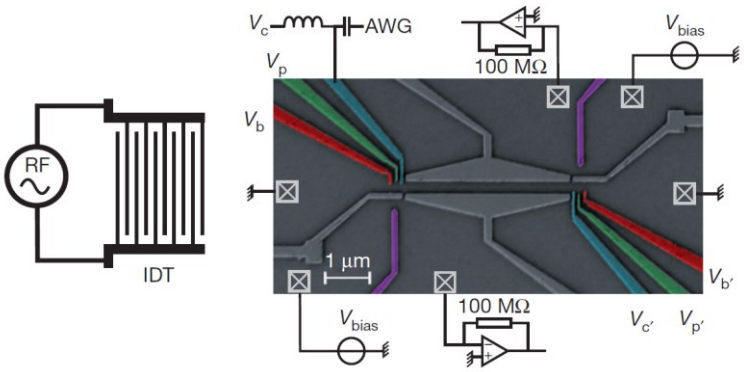

Figure 1.3.3: SEM image of the single-electron transfer device with a circuit diagram of the experimental setup. Reprinted by permission from Springer Nature Customer Service Centre GmbH: [63].

transferred to the right one isolated by a one-dimensional channel with a few micro meters (see Fig. 1.3.3). Currently, a big effort is put into the higher fidelity of the single electron transport process [65].

The quantum nature of SAW is another important issue in mesoscopic physics. The SAW is a mechanical wave and can be regarded as a classified phonon. For the observation of the quantum nature, it is reasonable to make the SAW interact with an artificial atom which has the discrete energy levels. The interaction between the SAW and the artificial atom generates the superposition of the phonon state and the eigenstate of the artificial atom. Such an interaction has been observed in the double quantum dot system [66, 67] and the superconducting qubit [68, 69]. Especially, the experiments using the superconducting qubit have extensively been investigated because of the good controllability. So far, several quantum phenomena have been observed, such as strong coupling states [70, 71] and Fock-states [72].

The propagation speed of sound in solids is five orders of magnitude slower

than for light. The slow propagation allows for manipulation of acoustic signals on-chip. This causes the intrinsic time delay, which could in the future result in interesting new functionalities in quantum information in future [73].

1.3.3 Modulation of the electronic properties of atomically thin film by SAWs

Up to now, SAW experiments have been extended to the integration of SAWs and 2D materials such as graphene [73]. The 2D material can be mechanically exfoliated down to an atomically thin film by the scotch tape method (see Sec. 2.2) [74]. Thanks to its thinness, the electronic properties of the thin film are considered to be modulated by the SAW: the electrostatic potential or the strain on the surface of the piezoelectric substrate can modulate the electronic properties of the thin film. The interactions between the SAW and 2D materials provide an exciting test-bed to study new phenomena [75].

Recently, acoustic charge transport in the semiconducting thin films such as graphene [16, 76], MoS_2 [15, 77, 78], and black phosuphrous [79, 80] has attracted much attention. By irradiating the SAW on the piezoelectric substrate, the carrier are trapped or propagated by the electrostatic potential at the speed of sound. The acoustoelectric current in the device can be tuned by modulating the carrier density of the thin film using a gate voltage [81, 82]. These semiconducting thin films are particularly attractive for optoelectronics because of the inherent bandgaps. Thus, the integration of the SAW in such semiconducting thin films would provide a new device functionality such as the highly sensitive sensors [73].

1.3.4 Integration of SAW and superconducting thin film

In fact, the SAW has been used as a probe to investigate the superconductivity in terms of ultrasonic absorption [8]. Akao measured the attenuation of the SAWs propagating under thin films of In and Pb deposited on the quartz substrate [83]. They obtained the temperature dependence of attenuation predicted by BCS theory. Kratzig *et al*. studied the attenuation of the SAWs propagating under a Pb thin film and revealed the existence of a critical magnetic field originated from the surface superconductivity [84]. They also investigated the interaction between the SAWs and a bilayer structure composed of a metal and a superconducting thin film. This revealed the existence proximity effect of the superconductivity into the metal layer [85].

Contrary to the above previous studies on the SAW and superconducting thin film, we focus on the modulation of the electronic properties of the superconducting thin film. For this purpose, we have utilized $NbSe_2$ and NbS_2 as superconducting thin films. The origin of the BCS superconductivity is the electron-phonon interaction [8]. If the superconductors are atomically thin, the electronic properties of atomically thin films is expected to be modulated by the SAW. Especially, $NbSe_2$ is interesting because of its CDW phase, which is also originated from the electron-phonon interaction.

In the next chapter, we will explain the experimental details to perform the electrical transport measurement using the superconducting thin films exposed to the SAW.

Chapter 2

Experimental details

In this chapter, we describe experimental details on our SAW devices and superconducting thin films. Firstly, we review fundamental properties of the SAW (Sec. 2.1). Secondly, we present the recent progress on atomically thin superconducting film devices (Sec. 2.2). Thirdly, we explain our fabrication methods and an experimental setup (Sec. 2.3 and Sec. 2.4).

2.1 Technical description of SAW devices

2.1.1 Piezoelectric materials

Generally, strain S in a solid responses to mechanical stress T. The mechanical stress, of whose unit is $\mathrm{N/m^2}$, is the force applied per unit area of the solid. The strain is the fractional deformation due to the mechanical stress. The strain can be defined as the ratio of the fractional deformation δL and the initial length L: $S = \delta L/L$, so the strain is a dimensionless value. Because the strain and the stress are vector quantities, the relation between them can be written using forth-order

elastic compliance tensor $s_{E,\,ijkl}$ as follows:

$$S_{ij} = s_{E,ijkl} T_{kl}. \tag{2.1}$$

When an electric field is applied to a non-piezoelectric dielectric, the dielectric polarization is induced. The relation between the electric displacement D and the electric field E is given by:

$$D_i = \varepsilon_{T,ij} E_j, \tag{2.2}$$

where $\varepsilon_{T,ik}$ is the second-order dielectric constant tensor.

The simple relations described above no longer holds in a piezoelectric material. Due to the electro-mechanical coupling, the electric field induces the mechanical strain and vice versa. These relations in the linear response regime can be described by:

$$S_{ij} = s_{E,ijkl} T_{kl} + d_{kji} E_k \tag{2.3}$$

$$D_i = d_{ikl} T_{kl} + \varepsilon_{T,ik} E_k, \tag{2.4}$$

where d_{kji} denotes the piezoelectric constant tensor and $i, j, k, l = 1, 2, 3$ denote a coordinate basis. The piezoelectricity of a crystal is defined by the crystal structure. When the crystal has a piezoelectricity, the piezoelectric constant tensor d_{kji} has a finite value.

To induce a SAW, an electromechanical coupling coefficient K^2 of the crystal is important. It is defined using the piezoelectric constant d, elastic compliance s

and dielectric constant ε:

$$K^2 = \frac{d^2}{s\varepsilon}. \tag{2.5}$$

The electromechanical coupling coefficient depends on the piezoelectric material, the crystal cut, and the propagation direction of the SAWs.

2.1.2 $LiNbO_3$

There are several piezoelectric crystals. Representative piezoelectric crystals are, for example, quartz, $LiNbO_3$, $LiTaO_3$ and $Li_2B_4O_7$. In these crystals, $LiNbO_3$ has a relatively large electromechanical coupling coefficient $K^2 \sim 5.3$ % and is suitable for wideband filters.

Zachariasen first synthesized and described $LiNbO_3$ in 1928 [86]. Matthias *et al*. succeeded in growing the $LiNbO_3$ crystal by the flux method [87]. Since a report on the growth of large single crystal with the pulling method by Ballmann [88], the fundamental properties of $LiNbO_3$ and its applications have been extensively investigated as a representative ferroelectric material. Nassau *et al*. [89,90] investigated the growth of single crystal and the poling treatment [89,90]. Abarahams *et al*. measured the crystal structure by the X-ray diffraction and the neutron diffraction [91–93]. A large piezoelectric effect of the single crystal $LiNbO_3$ was quite attractive for researchers [94]. The SAW devices have been implemented in electrical devices since the late 1970s. Currently, SAW devices are found in many electrical devices. The SAW devices are applied as delay lines, bandpass filters, resonators and so on [49].

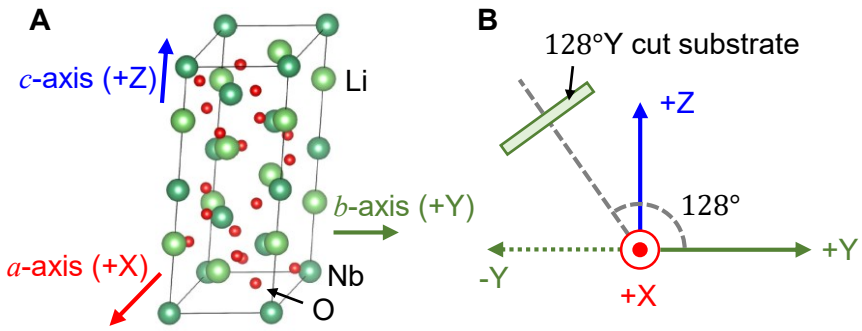

Figure 2.1.1: (A) Crystal structure of $LiNbO_3$. The figure is illustrated by using VESTA [95]. (B) A schematic image of the $LiNbO_3$ substrate with the crystal cut of 128° Y.

The crystal structure of $LiNbO_3$ is shown in Fig. 2.1.1. The $LiNbO_3$ crystal is trigonal. When the temperature is higher than the critical temperature $T_C \sim 1530\ K$, $LiNbO_3$ is paraelectric and its point group is $\bar{3}m$. Below T_C, $LiNbO_3$ is ferroelectric and its point group is $3m$. $LiNbO_3$ shows the piezoelectric effect and pyroelectric effect, as described later.

The velocity of the SAW with various crystal cuts is investigated experimentally and theoretically, as shown in Fig. 2.1.2. [94]. In this graph, the propagating direction of the SAW is the X-axis. The vertical axis is a rotating angle from the $+$Y axis to $-$Y axis via $+$Z axis as shown in Fig. 2.1.2. The Rayleigh mode generated at the surface of a $LiNbO_3$ substrate takes a maximum values at an electromechanical coupling coefficient K^2 and a wave velocity when the crystal cut is 128° Y. In this crystal cut, the diffusion of the SAWs into the bulk is minimum [94]. Based on these properties, we have chosen $LiNbO_3$ (128° Y) as a piezoelectric substrate.

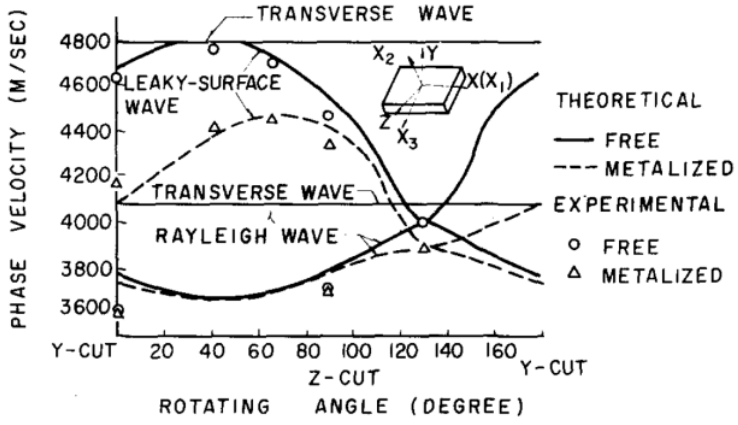

Figure 2.1.2: Velocities of two kinds of transverse waves, Rayleigh and leaky surface waves as a function of the rotating angle θ. Reprinted from [94], with the permission of AIP Publishing.

2.1.3 *S*-parameter

In general, an impedance or an admittance is measured to evaluate the low frequency properties of electrical circuit. In the higher frequency regime than sub-GHz, however, it is difficult to measure the current and the voltage directly. Thus, it is also difficult to obtain the impedance or the admittance. For the evaluation of the electrical properties in the high frequency regime, it is convenient to measure the electric power. The high frequency properties can be evaluated by the ratio of the input power to the output power. Scattering parameters (*S*-parameters) describes the relation between them.

Let us consider the two-port network which is composed of the scatter connected by the two leads (port 1 and port 2) as shown in Fig. 2.1.3. We define the input current and the input voltage from port n ($n = 1,\ 2$) as I_{n+} and V_{n+}, respectively. We also define the output current and the output voltage as I_{n-} and V_{n-},

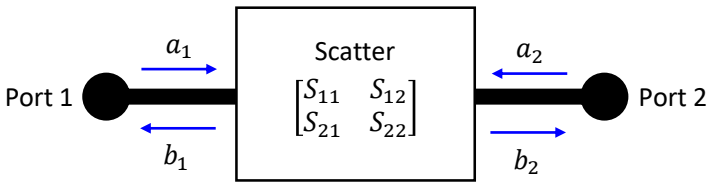

Figure 2.1.3: A schematic image of the two-port network.

respectively. Then, by using these parameters, the physical quantities which relate to the electric power can be described as follows:

$$a_n = V_{n+}/\sqrt{Z_0} = I_{n+}\sqrt{Z_0}\ \text{(input)} \tag{2.6}$$

$$b_n = V_{n-}/\sqrt{Z_0} = I_{n-}\sqrt{Z_0}\ \text{(output)}, \tag{2.7}$$

where Z_0 denotes the characteristic impedance, which is 50 Ω in the field of *rf* engineering. The fact that the squares of a_n and b_n have the electric power dimension indicates that these physical quantities are related to the power. The *S*-parameters can be defined as follows:

$$\begin{bmatrix} b_1 \\ b_2 \end{bmatrix} = \begin{bmatrix} S_{11} & S_{12} \\ S_{21} & S_{22} \end{bmatrix} \begin{bmatrix} a_1 \\ b_2 \end{bmatrix}, \tag{2.8}$$

where a_n and b_n are complex values and contain the information of the phase. As can be seen in Eq. (2.8), S_{11} and S_{22} denote the reflectance and S_{21} and S_{12} denote the transmittance of the microwave.

2.1.4 Frequency response of IDTs

The delta function model is the simplest model which provides basic information on the *S*-parameters of SAW filter [96]. We consider the uniform interdigital transducers which are assumed to be non-reflective. We also assume the ideal propagation conditions where the propagation loss and diffraction can be ignored. This model cannot provide information on filter input-output impedance levels, circuit factor loading, bulk wave interference or diffraction. This model yields only relative insertion loss as a function of frequency. Despite these limitations, it can provide excellent preliminary design information on the response of SAW devices. In the following mathematical deviations, we have ignored the bidirectional nature of the IDTs because the absolute values of insertion loss cannot be predicted.

The delta function model approximates the complex electric field between adjacent two fingers of IDT as a delta function source. Although the real distribution of the time-varying electric field under adjacent electrodes is quite complex, we have approximated it, normal to the piezoelectric surface.

Let us consider the input IDT with a response function of $H_1(f)$. As depicted in Fig. 2.1.4, the center-center distance is $\lambda_0/2$ and the center frequency is $f_0 = v_{SAW}/\lambda_0$ (Fig. 2.1.4 (A)). The time-dependent input voltage induces the instantaneous charge accumulation on adjacent electrode fingers. Adjacent electrodes have opposite voltage polarity and opposite charge accumulation. The electric field induced by the accumulated charge can be modeled as a delta function source at the center of each finger (Fig. 2.1.4 (B)).

The spatially-distributed delta function contributions can be superposed at a

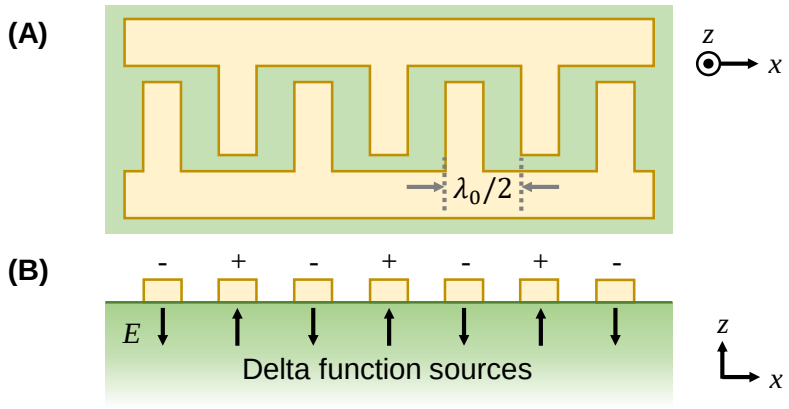

Figure 2.1.4: (A) IDT with uniform finger spacing and constant finger overlap. (B) Delta-function model of electric field distribution under excited IDT, with one sources under each excited electrode.

reference point along the x-axis. Here, we assume the IDT has the odd number N of electrodes for simplicity. The summation of sources yields the frequency response $H_1(f)$. Although the amplitudes of the delta sources are uniform, the individual phase angles at the reference point should depend on the distance x_n from each source to this reference point. The resultant frequency response is given by

$$H_1(f) = \sum_{n=-(N-1)/2}^{(N-1)/2} (-1)^n e^{-jkx_n}, \tag{2.9}$$

where the term $(-1)^n$ relates the alternating electrode polarity, and e^{-jkx_n} denotes the phase shift for the electrode located at x_n. This summation (Eq. (2.9)) can be described by a cosine series: $H_1(f) = 1 + 2\cos(\pi\frac{f-f_0}{f_0}) + \cdots + 2\cos(N_\mathrm{p}\pi\frac{f-f_0}{f_0})$, where $N_\mathrm{p} = (N-1)/2$ represents the number of electrode finger pairs. Close to

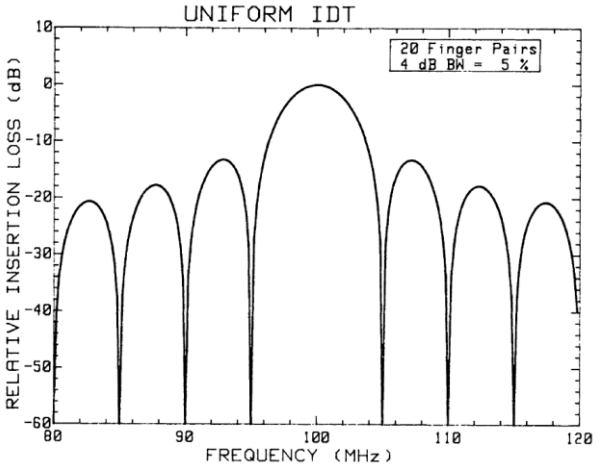

Figure 2.1.5: Calculated magnitude response $|H_1(f)|$ of uniform IDT with $N_\mathrm{p} = 20$ and $f_0 = 100$ MHz. Reprinted from [50], with permission from Elsevier.

f_0, this equation approximates a sinc function response given by

$$|H_1(f)| \sim N\left|\frac{\sin(N_\mathrm{p}\pi(f-f_0)/f_0)}{N_\mathrm{p}\pi(f-f_0)/f_0}\right| \tag{2.10}$$

$$= \left|\mathrm{sinc}(N_\mathrm{p}\pi(f-f_0)/f_0)\right|. \tag{2.11}$$

Figure 2.1.5 shows a calculated $|H_1(f)|$ for the input IDT as a function of f with $N_\mathrm{p} = 20$ and $f_0 = 100$ MHz. We can see that the first sidelobes are -12 dB below the main peak at the center frequency. This level is characteristic of sinc function responses.

Using the same method, the frequency response $H_2(f)$ of the output IDT is obtained. The total amplitude response is given by $|H(f)| = |H_1(f)| \cdot |H_2(f)|$. Figure 2.1.6 shows typical frequency responses of the IDTs measured by a network analyzer (Keysight, E5071C). The IDTs fabricated on the $LiNbO_3$ substrate are designed for a wavelength $\lambda = 2\mu$m and $N_\mathrm{p} = 20$. Since S_{21} and S_{12} are pro-

portional to the product of each amplitude response, the responses are a square of sinc function. We can see the first sidelobes are -24 dB below the main peak at the center frequency. S_{11} and S_{22} show a dip structure at the resonance frequency. The characteristics of IDTs can also be evaluated by S_{11} or S_{22}. The resonance frequency in S_{11} and S_{22} is slightly different from the resonance frequency in S_{21} by $\sim$ 30 MHz. The difference corresponds to the difference of the wavelength $\sim$ 30 nm. This difference can occur due to the accuracy of the micro-fabrication.

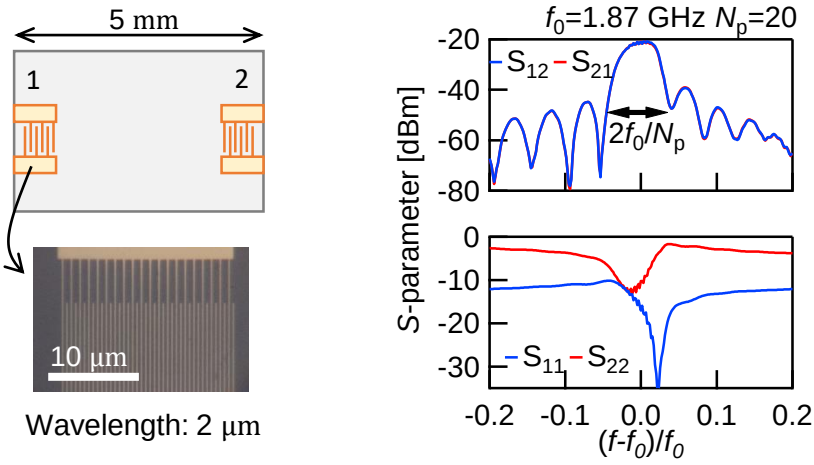

Figure 2.1.6: A schematic image (left top) and optical microscope image (left bottom) of the IDTs fabricated on the $LiNbO_3$ substrate. (Right) S-parameters measured for the IDTs.

2.2 Superconducting thin films

2.2.1 Layered materials

Since the discovery of graphene, a single layer of graphite, by Novoselov and Geim *et al*. in 2004 [97], a huge number of researches on 2D materials have been studied extensively. The discovery of graphene has generated many research fields from the fundamental properties to the applications [74, 98].

Followed by the great success of graphene, an identically big boom occurs in the fields of other 2D materials. The library of the 2D materials increase every year: two dimensional traditional metal dichalcogenides (TMDs) such as a semiconducting MoS_2 [10, 99–101] or a superconducting $NbSe_2$ [102–104], an insulating hexagonal boron nitride (hBN) [105–108], cupper oxides [9, 109–112] and ferromagnetic materials [113–115]. Depending on the crystal structure and the elemental composition, a thin film of 2D material is categorized to metal, semimetal, semiconductor, insulator or superconductor.

A TMD MX_2 is the first candidate of the "next graphene" materials. It is a compound of transition metal M and chalcogen X [116]. Most of TMDs are semiconductor inherently which has a potential to realize ultra-thin and low power consumption transistors. Whereas the band gap and the large carrier density is comparable to that of silicon, such TDMs can be transfered to a flexible substrate and is robust to a stress and a strain. The lattice of MX_2 has a laminated structure of unit layer (namely van der Waals heterostructure) composed of an M-layer sandwiched by two X-layers. The M-layer and X-layer are connected strongly by the covalent bonds while each unit layers, i.e. the bonding between the X-layers,

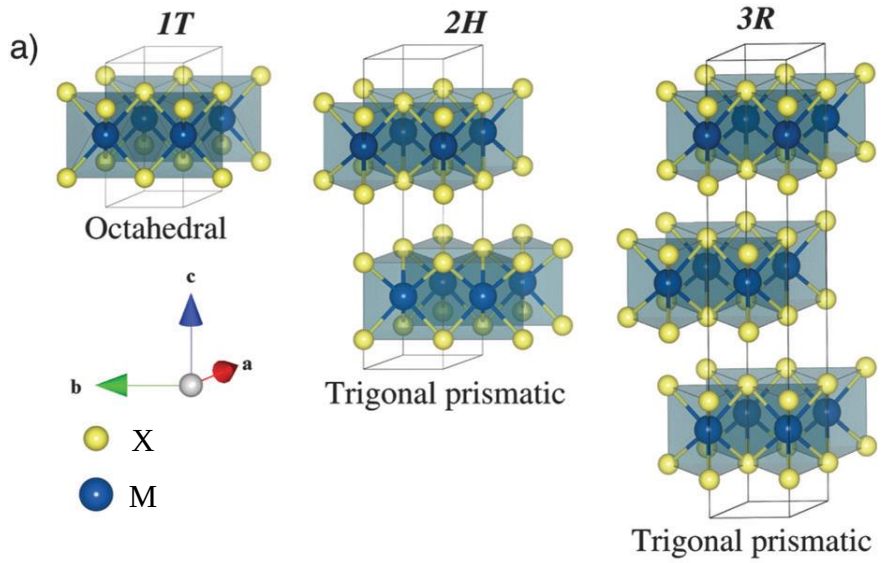

Figure 2.2.1: Structural representation of 1T, 2H and 3R TMD geometries together with their metal atom coordination. In this figure, the letters, X and M, stand for chalcogen and transition metal, respectively. [117] - Reproduced by permission of The Royal Society of Chemistry.

are weakly connected by the van der Waals force. There are two types of geometries in terms of the coordination of X atoms to M atom: octahedral geometry and triangular prism geometry. Because the stacking structure also has several patterns, TDMs have many kinds of geometries. In Fig. 2.2.1, we show several geometries of TDM, 1T, 2H and 3R. The numbers indicate the number of layers in the unit cell and the letters stand for trigonal, hexagonal and rhombohedral, respectively [117].

One of the most important breakthroughs in the field of TMDs is the modulation of electronic properties by a gate voltage [10]. To control the electronic properties, the modulation methods of the free carrier density, and thus the density of states near the Fermi surface, has long been required. Electrical gating is a

clean and reversible method for carrier doping near the surface of material [118]. Especially, an electric double layer using an ionic liquid has succeeded in doping various insulator surfaces into metallic phases [119, 120]. It has been difficult, however, to modulate the properties of metals due to the screening of the high carrier density [121]. Recent progress in atomically thin TMD has enabled to modulate the carrier density by gating [10]. This technique gives us the knowledge about many body systems including the coexistence of multi-orders [11,103,122], the Bose metal phase [123], the Ising paring in superconductivity [104]. The density of states (DOS) of the atomically thin film is sensitive to the gate voltage, which provides an ideal system to probe the effect of the electrical doping in the high carrier density regime.

In parallel with the efforts on 2D materials, another research field has emerged [74]. It deals with heterostructures made by stacking different 2D crystals on top of each other. The basic principle is that taking a monolayer, putting it on top of another monolayer or few-layer crystal and so on. The resulting stack represents an artificial material assembled in a chosen sequence. Recent experiments has been demonstrated the possibility of making multilayer van der Waals heterostructures experimentally [124–127].

2.2.2 $NbSe_2$

2H-$NbSe_2$ is a representative TMD material which has a layered structure stacked by the van der Waals force. The crystal structure of 2H-$NbSe_2$ is described in Fig. 2.2.2. The lattice constants are $a = b \sim 3.4$ Å and $c \sim 12.6$ Å [32]. A monolayer $NbSe_2$ consists of an atomic layer of Nb and two layers of Se in the

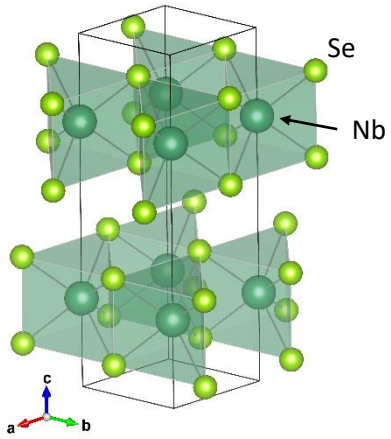

Figure 2.2.2: Crystal structure of 2H-$NbSe_2$. The figure is drawn by VESTA [95].

trigonal prismatic structure. Bulk 2H-$NbSe_2$ is formed by stacking monolayers of $NbSe_2$ with adjacent layers rotated by 180° with respect to one another.

As shown in Fig. 2.2.3, the bulk $NbSe_2$ have three Fermi surfaces around the Γ point and two Fermi surfaces around the K point [128–130]. $NbSe_2$ is a hole metal in room temperature [18].

The CDW in TMD is one of the most extensively investigated topics in condensed mater physics together with superconductivity [37]. $NbSe_2$ is one of the most widely investigated model systems as 2D CDW. The intriguing nature of the CDW in $NbSe_2$ has become a long term mystery because of the complicated CDW structure [116]. In the CDW phase of $NbSe_2$ (below 33 K), selenium atoms have a periodic modulation that is three times the lattice constant for selenium atoms. Moncton *et al.* showed that the structural transformation to the triple-q CDW with some incommensurability takes place in $NbSe_2$ by performing neutron diffraction measurements [32, 131]. Other TMD materials, such as 2H-$TaSe_2$ and 1T-TaS_2, are known to show the ICDW-CCDW transition with decreasing the

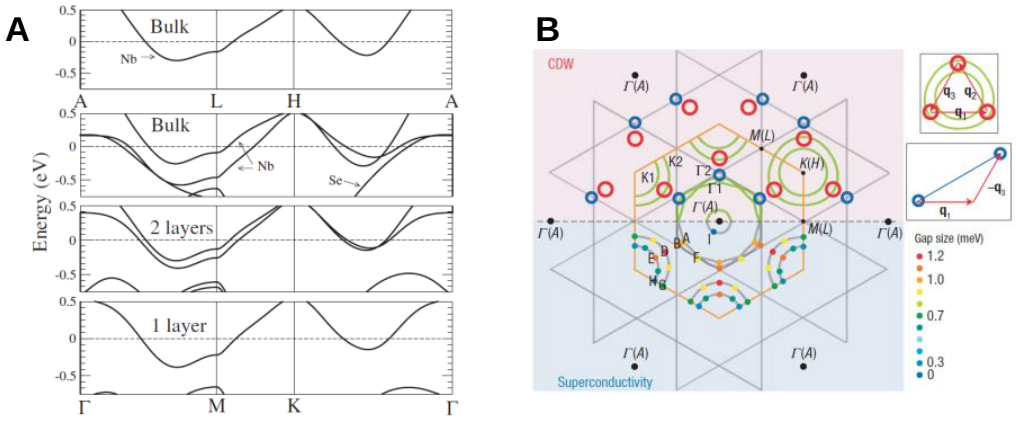

Figure 2.2.3: (A) Electronic band structure of bulk, bilayer, and monolayer 2H-$NbSe_2$ around the Fermi energy. Reprinted figure with permission from [133] Copyright 2020 by the American Physical Society. (B) Fermi surface of bulk $NbSe_2$ [128]. (identifications of Fermi surface sheets: Γ1, Γ2, K1 and K2). Symmetric arrangement of the two spots (red and blue circles, upper half) in the first BZ (orange hexagon). The Fermi surface, determined by angle-resolved photoemission spectroscopy (green curves), shows that primary CDW vectors (q_1, q_2, q_3) lie on K2 and connect red circles, whereas secondary CDW vectors ($q_i \pm q_j$) with $i, j = S1, 2, 3$ connect blue circles. Superconducting-gap values are mapped with a colour scale (lower half). Reprinted by permission from Springer Nature Customer Service Centre GmbH: [128].

temperature [32, 131]. So, $NbSe_2$ was also expected to show the ICDW-CCDW transition. However, the CCDW phase does not appear in $NbSe_2$ even at low temperature [32, 131, 132].

On the other hand, a discommensurate CDW (DCDW) structure has been indicated by the electron microscopy studies [134] and the NMR studies [135, 136]. In the DCDW state, orthorhombic CCDW domains are locally formed and the adjacent domains are connected by a phase slip. A recent STM study has directly observed the DCDW structure and revealed that there are several types of domains with a size of about 10 nm in the equilibrium $NbSe_2$ [137]. A typical STM image of $NbSe_2$ is shown in Fig. 2.2.4. There are several types of CDW structures:

the CDW has its maxima on cation (Nb), anion (Se) or hollow sites. However, only two types can be observed: the anion-centered (AC) structure (gray region) and the hollow-centered (HC) structure (colored region). The color and number indicate particular HC-CDW domains among nine translationally degenerate domains. The AC domain between two HC domains play a role in the phase slip by a single unit cell $a \sim \lambda_{\mathrm{CDW}}/3$. However, they very rarely observed the single-q phase. This is contradict to in other STM researches [138]. So, the microscopic origin of the CDW transition and the CDW structure of $NbSe_2$ are still under debate.

In addition to the CDW transition, a superconducting transition takes place in $NbSe_2$ at 7.2 K. This provides us an interesting situation where the CDW and superconductivity coexist. The competition of the superconducting phase and the CDW phase has interested us for a long time. $NbSe_2$ is considered to be a strong electron-phonon coupling material [139]. In such a material, the relative stability between the two phases depends on the three basic parameters: the hopping rate between two neighboring orbitals, the electron-phonon interaction, and the frequency of phonon [140]. At the Fermi surface of $NbSe_2$ around the K point, the CDW order and the superconducting order coexist. New phenomena may be expected to arise due to the coupling between them. In fact, it was reported that new Raman active modes appear when the system becomes superconducting [141, 142]. These modes are close in energy to the superconducting gap. The applied magnetic field suppresses the intensity of the Raman active modes and enhance the intensity of the CDW-induced modes. Thus, they provided evidence that the new modes result from a coupling between the CDW and superconductivity.

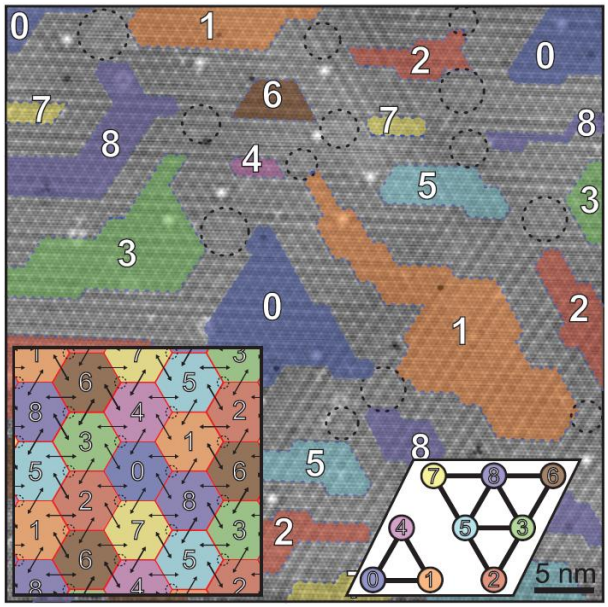

Figure 2.2.4: Scanning tunneling microscope (STM) topography of HC CDW domains in 2H-$NbSe_2$. Black dashed circles indicate the region of AC CDW dislocations. The colors and numbers indicate particular HC CDW domains among nine translationally degenerate domains. These domains have to be connected properly in the ideal domain network shown in the insets. Different domains are identified by their relative translation as defined in the right inset within one CDW unit cell. The black arrows represent the directions of CDW translations among HC CDW domains. Reprinted figure with permission from [137] Copyright 2020 by the American Physical Society.

Currently, it is considered that the coupling between the CDW and superconductivity considered arises from the modulation of the density of states at the Fermi energy level by the amplitude mode of the CDW [143–147].

2.3 Fabrication

2.3.1 Device fabrication

For fabrication of SAW devices and superconducting thin films, micro fabrication techniques with sub-micron order are necessary. In this section, we describe an overview of the device fabrication methods.

An electron beam (EB) lithography is used for micro-fabrication. SAW and thin film devices are fabricated on a $LiNbO_3$ substrate (Crystal Base, 128 ° Y) which is explained in Sec. 2.1.2. The first step for micro-fabrication is to clean the substrate with the organic compound liquid such as acetone and isopropyl alcohol. The cleanness of the substrate surface strongly affects to the yield ratio of the device fabrication. Ozone ashing process (SAMCO, UV-1) is another effective method to make the surface clean. The ashing process removes dusts composed of organic compounds. Typically, the ashing time is 10 min with a temperature of 120 °C.

As a next step, atomically thin films are fabricated on the substrate by the mechanical exfoliation technique, which is the so-called scotch tape method [74]. The scotch tape exfoliation should be done in a glove box, where an inert gas (in the present case, Ar gas with a purity of 99.9999%) is filled, in order to avoid any degradation of the thin film by, for example, O_2 and H_2O in the ambient condition [148]. Metallic thin film TMDs are quite sensitive to O_2 and H_2O. That is why we should avoid to handle thin film devices out of the glove box without any coating such as EB resist. $NbSe_2$ [149] and NbS_2 (HQ Graphene) are used as superconducting layered materials. As detailed in the previous section, the

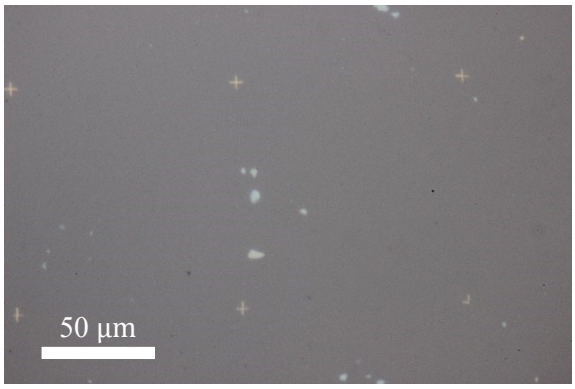

Figure 2.3.1: Optical microscope image of the $NbSe_2$ thin films rubbed onto the $LiNbO_3$ substrate.

former has both the superconductivity and the CDW state while the latter has only the superconducting phase. The atomically thin films are obtained by repeatedly mechanical exfoliations of the flake, which are peeled from the bulk crystals with scotch tape (3M). The flakes are transferred to the masking tape (Nitto Denko) with less glue. Finally, the masking tape is pasted on the substrate, and then the flakes are rubbed onto the substrate, as shown in Fig. 2.3.1.

In this process, there are a huge number of flakes on the $LiNbO_3$ substrate but we can use only one flake. Only one set of IDTs can be fabricated for one substrate because the high frequency line takes a large area. So we need to choose a suitable flake. In this experiment, we choose the flake with a thickness of about 30 nm. A thicker flake has a risk of stepwise break of an electrode for contact. A thinner flake is more fragile to the atmosphere, which results in degradation even within a short handling time, for instance, during wire bonding. Most of the improper flakes can be sorted out by ultrasonic cleaning. The substrate is immersed in acetone packed in a glass bottle with the Ar ambient condition and cleaned with an ultrasonic cleaner. We choose a suitable flake from the remained

flakes. The flake used in this experiment should be located around the center of the substrate and should be isolated from the other flakes because the IDTs should be fabricated around the flake.

We then coat EB resist on the $LiNbO_3$ substrate. In our case, the EB resist is a polymethyl-methacrylate (PMMA, 950 A4, MICROCHEM) resist. The PMMA resist is coated on a $LiNbO_3$ substrate by using a spin coater (MIKASA, MS-A100) and is baked to dry out the solvent at 150 °C for 10 min. The espacer (Showa Denko, 300Z) is also coated on the substrate. Because $LiNbO_3$ is an insulator, electrons emitted to the substrate cannot run away from the substrate. Thus the expacer, which is an electrically conductive macromolecule, enable us to prevent the charging effect.

The pattern of electrodes is designed using VectorWorks (Nemetschek Vectorworks) which is a general-purpose CAD software. The widths of the contact electrodes are typically sub-micron for the voltage probes and several microns for the current sources. The electrodes for voltage probes should be narrow to make it easier to define the distance between the two probes. The electrodes for current source and drain should be wider to flow a homogeneous current into the sample. A wavelength of SAWs can be defined by the pitch of finger-shaped electrode in the IDT. The resonance frequency of the SAWs can be estimated from the following relation: $v_{\mathrm{SAW}} = f_{\mathrm{SAW}}\lambda_{\mathrm{SAW}}$. The electrodes are patterned by EB lithography (Elionix, ELS-7000) with the dose of 800 $\mu\mathrm{C}/\mathrm{cm}^2$. The field correction for the EB lithography is performed using cross marks prepared before using EB lithography.

Here, we mention the method to evaluate the thickness of the film on the sub-

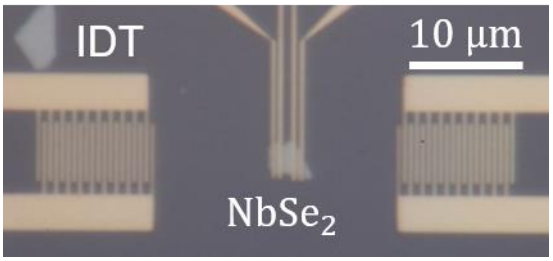

Figure 2.3.2: Optical microscope image of a typical $NbSe_2$ SAW device.

strate. The thickness is measured by a commercially available atomic force microscope (AFM, Hitachi Hightech. AFM5200S). It should be noted that the substrate the PMMA and the espacer are coated during the AFM measurement to prevent degradation of the thin film. In addition, due to the transparency of the $LiNbO_3$ substrate, the detector of the laser in the AFM to observe the oscillation of the beam is interfered by the reflection of the laser from the substrate. So, the coating of the PMMA and the espacer is necessary. Although we did not measure the thickness of the flake directly, the thickness can be estimated even with the PMMA resist.

In order to remove the espacer, the $LiNbO_3$ substrate is rinsed with distillated water for 30 sec. For the development, the substrate is immersed in the developer for PMMA (Isopropyl alcohol: Methyl isobutyl ketone=3:1) for 60 sec and rinsed by isopropyl alcohol for 20 sec. Then the substrate is transferred into a vacuum chamber for depositions of Ti and Au. Here Ti is fist deposited by a thickness of 40 nm, and Au is then deposited by a thickness of 60 nm. To avoid a stepwise break for electrodes, the substrate is tilted by several degrees from the normal deposition. After the deposition, the substrate is immersed in acetone overnight for the lift-off process. Then the desired device can be obtained.

Figure 2.3.2 shows the optical microscope image of a typical $NbSe_2$ SAW device. The $NbSe_2$ flake has 5 μm in length, 2 μm in width and in 30 nm thickness. The pitch of the IDTs is designed so that the SAWs wave length is 1 μm. The resonance frequency is about 3 GHz.

2.3.2 Pyroelectricity of $LiNbO_3$ substrate

Because of the ferroelectricity of $LiNbO_3$ [150], $LiNbO_3$ substrates should be treated carefully. As detailed in [151], micro devices on the ferroelectric substrate can easily be broken by electric charges with increasing (or decreasing) temperature. The schematic images of the pyroelectrisity are shown in Fig. 2.3.3. Due to the dielectric polarization in the $LiNbO_3$ substrate, ionized gasses in the ambient condition are absorbed on the surface of the substrate. The screening by the ionized gasses stabilizes the surface electrostatically. In such a situation, a temperature change modifies the dielectric polarization and destabilize the surface state. The electrostatically unbalanced state locally induces a high voltage to the substrate, resulting in the breaking of microfabricated devices on the $LiNbO_3$ substrate.

The pyroelectricity of $LiNbO_3$ substrate decreases the production yield of the SAW devices. In the present experiment, many efforts have been made to avoid the electro-statically unbalanced state on the surface of $LiNbO_3$substrate: especially in the cooling process during the measurement and in the baking process of the PMMA resist. One of the effective ways is to treat the devices in an inert gas such as He and Ar. Such a less ionized gas suppresses the pyroelectricity. In the low temperature measurement, the sample space is always cleaned by the He gas

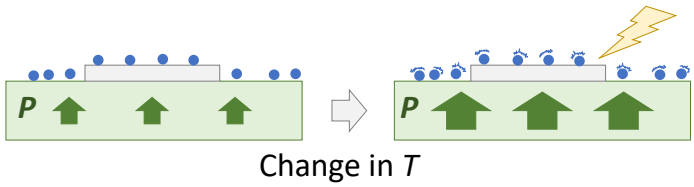

Figure 2.3.3: Schematic image of pyroelectricity. The dielectric polarization $\boldsymbol{P}$ (green arrows) are modified by changing in temperature T.

by the pump and flash method using a turbo molecular pump before the cooling process. In the baking process, on the other hand, the method has not been well established at the moment. Baking the PMMA resist in the Ar gas atmosphere for example in a glove box seems to be a good strategy. However, it does not suppress the pyroelectricity. That is why any baking process should be avoided after the microfabrication narrower than 1 μm: such narrow electrodes and IDTs are fragile to the static electricity.

2.4 Experimental setup

A schematic image of the measurement setup is shown in Fig. 2.4.1. Low temperature transport measurements of the SAW devices are performed using a refrigerator (Cryomagnetics, C-mag Vari-9) with a superconducting magnet up to 9 T. The brown line and the blue square part indicate the 1.6 K stage and the sample holder in the refrigerator, respectively. The measurement line consists of twenty low frequency lines for a standard four terminal measurements and four high frequency lines to control the SAWs. In the low frequency lines, constantan (gray lines) and copper (red lines) twisted wires are used from room temperature to the1.6 K stage and from the 1.6 K stage to the sample holder, respectively. For each low frequency line, a low pass filter (LPF) is attached at the 1.6 K stage. In this setup, a π filter is adopted for the LPF. The π filter consists of shunt capacitors (22 pF) and a resistance (10 Ω). The LPF is quite important to eliminate the external radiation which suppresses the superconducting transition temperature of thin films [152]. For the high frequency lines, the semi-rigid coaxial cables (green cylinder shaped symbol) are wired from room temperature to the sample holder via the attenuators (ATTs) at the 1.6 K stage, in order to reduce any noise from the outside. The typical attenuation of the ATT is 10 dBm.

In *dc* measurements, the bias current is generated by using a voltage source (Yokogawa, 7651) and a large resistance ($\sim$ 1 MΩ). The obtained *dc* voltage is measured by a digital Multimeter (Keythley, 2000). On the other hand, *ac* measurements with a Lock-in amplifier (Stanford Research System, SR830) are performed to obtain a differential resistance. The fundamental properties of the IDTs are obtained by measuring *S*-parameters using a network analyzer (Keysight,

E5071C). The SAWs are induced by a microwave generated from a signal generator (Agilent, N5171B).

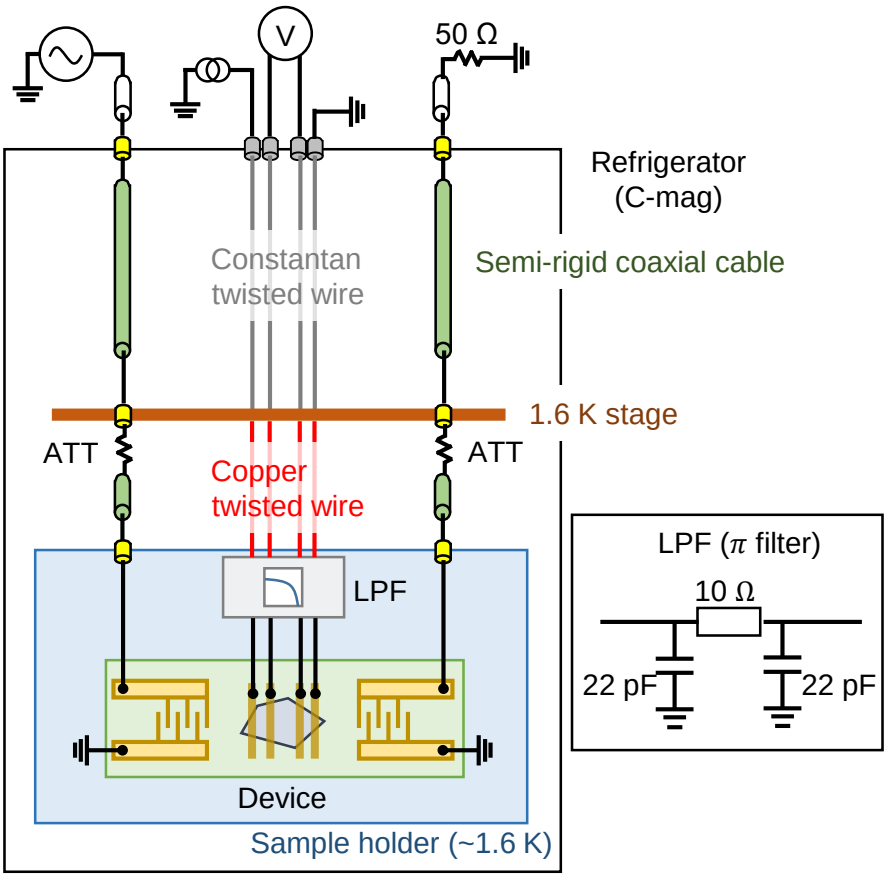

Figure 2.4.1: Schematic illustration of the measurement setup (left) and the circuit diagram of LPF (right).

Chapter 3

Negative resistance in superconducting $NbSe_2$ induced by SAW

In this chapter, we show experimental results on transport measurements in atomically thin superconducting films irradiated by SAWs [17]. First, we explain some fundamental properties of our IDTs and superconducting thin film devices. These measurements are performed to confirm the qualities of the device (Sec. 3.1). Then, we conduct transport measurements of the superconducting thin film devices with an irradiation of SAWs. The superconducting $NbSe_2$ devices show non-trivial features (Sec. 3.2). In Sec. 3.3, we briefly summarize the experimental results.

3.1 Fundamental properties of SAW and superconducting film devices

3.1.1 Characterization of SAW on $LiNbO_3$ substrate

To induce SAWs on a $LiNbO_3$ substrate, we use IDTs and apply a voltage power with a frequency of the GHz range between two comb-shaped electrodes. The characteristics of the IDTs are evaluated by *S*-parameters measurements. The experimental setup is show in Fig. 3.1.1. The pitch of the IDTs is 1 μm so that the wavelength of SAWs becomes the same value. We set the sample in the sample holder which is thermally connected to the 1.6 K stage. The sample is wired by the coaxial cables to the network analyzer via the attenuators (ATTs) with -10 dBm attenuation for each line.

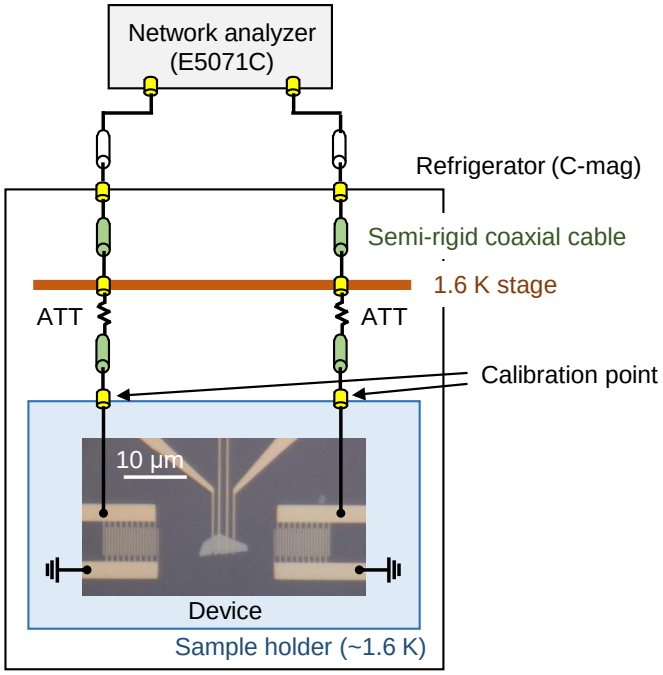

Figure 3.1.1: Optical microscope image of the SAW-superconducting film device.

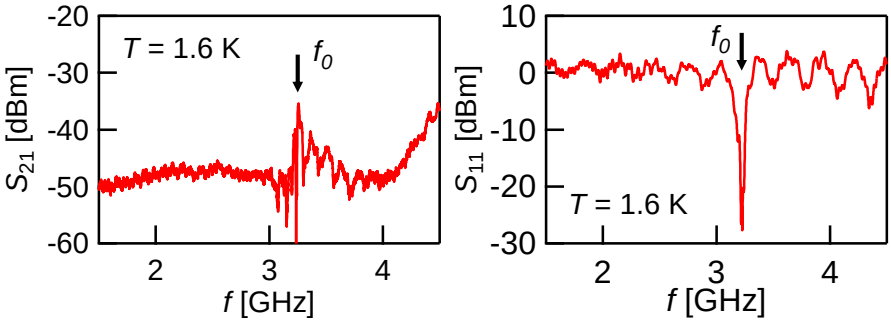

Figure 3.1.2: A typical *S*-parameter of IDTs measured by the network analyzer at 1.6 K. S_{21} (left) shows a peak and S_{11} (right) shows a sharp dip at 3.2 GHz. These indicates the resonance frequency f_0 of the SAW device.

The *S*-parameter is measured by a network analyzer (Keysight, E5071C) with a *rf* power of 0 dBm at the network analyzer. Figure 3.1.2 shows a typical characteristic of S_{21} and S_{11}. S_{21} corresponds to the transmittance of microwaves between the two IDTs and S_{11} corresponds to the reflectance of microwaves irradiated from one of the two IDTs (Sec. 2.1). In this measurement, the *S*-parameter from the network analyzer to the connector of the sample holder is already calibrated. Thus, the measured data (S_{21} and S_{11} shown in Fig. 3.1.2) should also reflect the *S*-parameters from the sample holder to the coplanar waveguide on the $LiNbO_3$ substrate. A peak in S_{21} and a sharp dip in S_{11} are observed at $f_0 \sim 3.2$ GHz. These indicate that the SAW is excited on the $LiNbO_3$ substrate. The resonance frequency is consistent with the designed value which can be estimated from the dispersion relation of the SAW: $v_{\mathrm{SAW}} = f_{\mathrm{SAW}} \lambda_{\mathrm{SAW}}$.

The *rf* power is expressed by dBm which is a unit of power normalized by 1 mW. The conversion of the unit between dBm and mW is expressed by the

following equation:

$$x = 10\log_{10}\frac{P}{1\ \mathrm{mW}}, \tag{3.1}$$

where P and x denote an arbitrary power P in mW and x in dBm, respectively. For example, -15 dBm corresponds to 30 μW. The depth in the S-parameter measurement (Fig. 3.1.2) is about -25 dBm, namely the power of reflectance is two orders smaller than the incident wave. This means that the *rf* power generated at the IDT is almost transferred to the power of the SAW. In general, SAWs are bidirectional [153] and there should be some energy loss due to the scattering by the electrodes. Accordingly, the actual power of the SAWs propagating on the superconducting thin film is smaller than the power estimated from the S_{11} property. However, it is not so important to discuss the exact power irradiation to the thin film.

In the present experiments, the maximum output *rf* power of the signal generator is -5 dBm. The reason is the following. The signal generator itself allows us to generate a power up to 30 dBm. When the *rf* power is higher than -5 dBm, it exceeds the cooling power of the refrigerator and the temperature increases. That is why our measurements are performed with lower *rf* powers than -5 dBm. We note that the high frequency lines include -10 dBm attenuation. Therefore, the *rf* power irradiated to the IDT is -15 dBm when the *rf* power is -5 dBm. The heating could be prevented by using the pulse excitation [50]. This would be the future work.

Now we estimate the lattice distortion amplitude modulated by the SAWs [54]. In the present work, the wavelength and the width of the SAW are $\lambda = 1\ \mu$m and $W = 5\ \mu$m, respectively. The characteristic admittance y_0 of the SAW

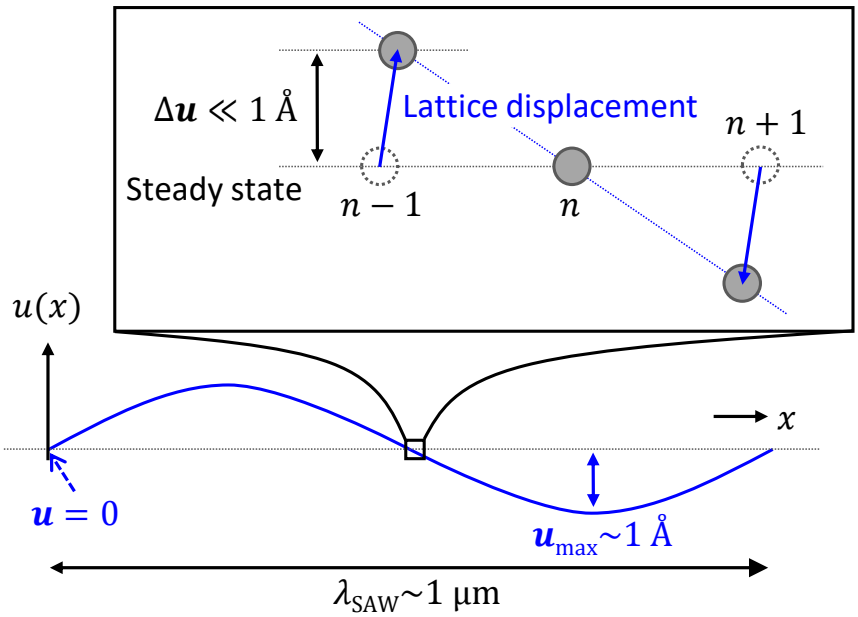

Figure 3.1.3: Schematic image of the displacement u. The maximum lattice displacement is sub Å. The difference of the displacements between the adjacent atoms is considerably small.

transmission-line, which is a unique value to the material of substrate, is defined as the power normalized by the width and the wavelength: $P = \frac{|\phi|^2}{2}\frac{W}{\lambda}y_0$. y_0 of the $LiNbO_3$ substrate (128 ° Y) is $y_0 = 0.21$ mS [54]. Hence the admittance and the impedance can be obtained as $Y_0 = y_0\frac{W}{\lambda} \sim 1.1$ mS and $Z_0 = 1/Y_0 \sim 900\ \Omega$. The relation between the power P and the electrostatic potential ϕ is given by $P = \frac{|\phi|^2}{2Z_0}$. For $P = 30\ \mu$W, $\phi = 0.23\ V$. The lattice displacements $u_{x,y,z}$ at surface are proportional to the electrical potential ϕ with coefficients $c_{x,y,z}$. It is known that $c_x = 0.1$ Å/V, $c_y = 2.0$ Å/V, $c_z = -1.8j$ Å/V for the $LiNbO_3$ substrate ($j^2 = -1$). Thus, the lattice displacement at surface can be estimated as $u_x = 0.02$ Å, $u_y = 0.46$ Å, $u_z = 0.41j$ Å. Here, it should be noted that the displacement $u_{x,y,z}$ is defined as the maximum difference at the surface from the

steady state (Fig. 3.1.3). Because adjacent atoms are displaced to the same direction, the displacement of the distance between two adjacent atoms is considerably small (< 1 Å). The atoms are displaced by $u_x = 0.02$ Å, $u_y = 0.46$ Å, $u_z = 0.41j$ Å during a quarter of wavelength $\lambda/4 = 250$ nm. Compared to the wavelength of the SAW, the lattice displacement is estimated to be at most 10^{-4}.

3.1.2 Characterization of atomically-thin superconducting films

To confirm the superconductivity of $NbSe_2$ and NbS_2 thin film devices, we performed the standard four-terminal lock-in measurement. The thickness of the superconducting thin films are about 30 nm as described in Sec. 2.3. Figure 3.1.4 shows the resistances of typical $NbSe_2$ and NbS_2 thin films on the $LiNbO_3$ substrate as a function of temperature. The resistance R is obtained by the standard *ac* lock-in technique. A broad kink structure due to the CDW transition is clearly observed at $T = 33$ K only for the $NbSe_2$ device. A sudden resistance drop due to the superconducting transition is also measured at $T_C = 7.2$ K. These results are well-established for bulk $NbSe_2$ samples [18, 102]. A similar superconducting transition takes place in the NbS_2 thin film device at 4 K. In contrast, it has no CDW phase [18], which is supported by the featureless temperature dependence of resistance. To evaluate the contact resistance between a superconducting flake and a Ti/Au electrode, we performed the two terminal measurement. The typical value of the contact resistances is about 100 Ω. The response of voltage is linear with the *ac* bias current up to 1 μA at least, demonstrating ohmic contacts at 1 μA.

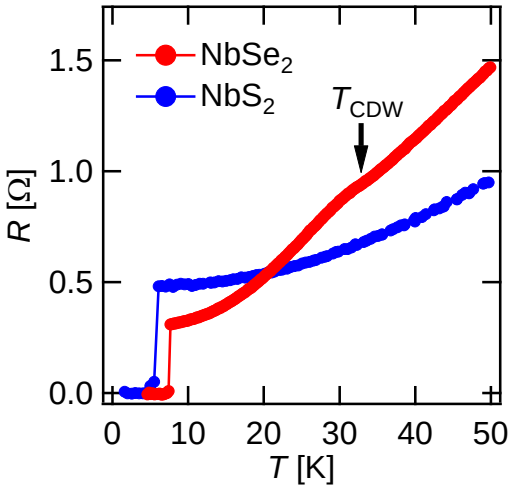

Figure 3.1.4: Temperature T dependence of the resistance R of a $NbSe_2$ (red) device and a NbS_2 (blue) device measured with the four terminal lock-in technique. The *ac* bias current is 1 μA. The arrow indicates the kink caused by the CDW transition which occurs only in the $NbSe_2$ at 33 K.

3.2 Experimental results

3.2.1 Current-Voltage properties under SAW irradiation

To evaluate the impact of the irradiation of SAW to atomically-thin superconducting films, we first measured current-voltage properties (I-V curves) of the $NbSe_2$ and NbS_2 thin films using the standard *dc* four terminal method (Figs. 3.2.1 A-H). Figures 3.2.1A and 3.2.1B shows the I-V curves of the $NbSe_2$ thin film measured with different *rf* powers. The shape of the I-V curve is a typical of overdamped Josephson junction [8] except for in the vicinity of zero bias current as shown in Fig. 3.2.1B (we will detail this point in the next paragraph). The critical current I_C for this device is about 0.8 mA, which is almost independent of the *rf* power up to 30 μW. This means that the superconductivity of the device is robust for the SAW irradiations. By numerically differentiating the I-V curve, the differential resistance dV/dI can be obtained as shown in Fig. 3.2.1C. The dV/dI around I_c slightly changes with the *rf* power (Fig. 3.2.1 C). This would be caused by the heating effect by the SAW irradiation.

A surprising property emerges in the I-V curves of $NbSe_2$ thin film within the bias current ± 50 μA (Fig. 3.2.1B). When the *rf* power is smaller than 1 μW, zero voltage is detected within the critical current. However, a finite voltage appears at ± 15 μA above the SAW power of 3 μW. Because the induced voltage is opposite in sign to the current, the slope at zero bias current, i.e., the differential resistance (or simply resistance) is negative. This indicates that the voltage drop is opposite to the bias current direction. The numerically obtained dV/dI is plotted in Fig. 3.2.1D as a function of I for different SAW powers. The negative differential

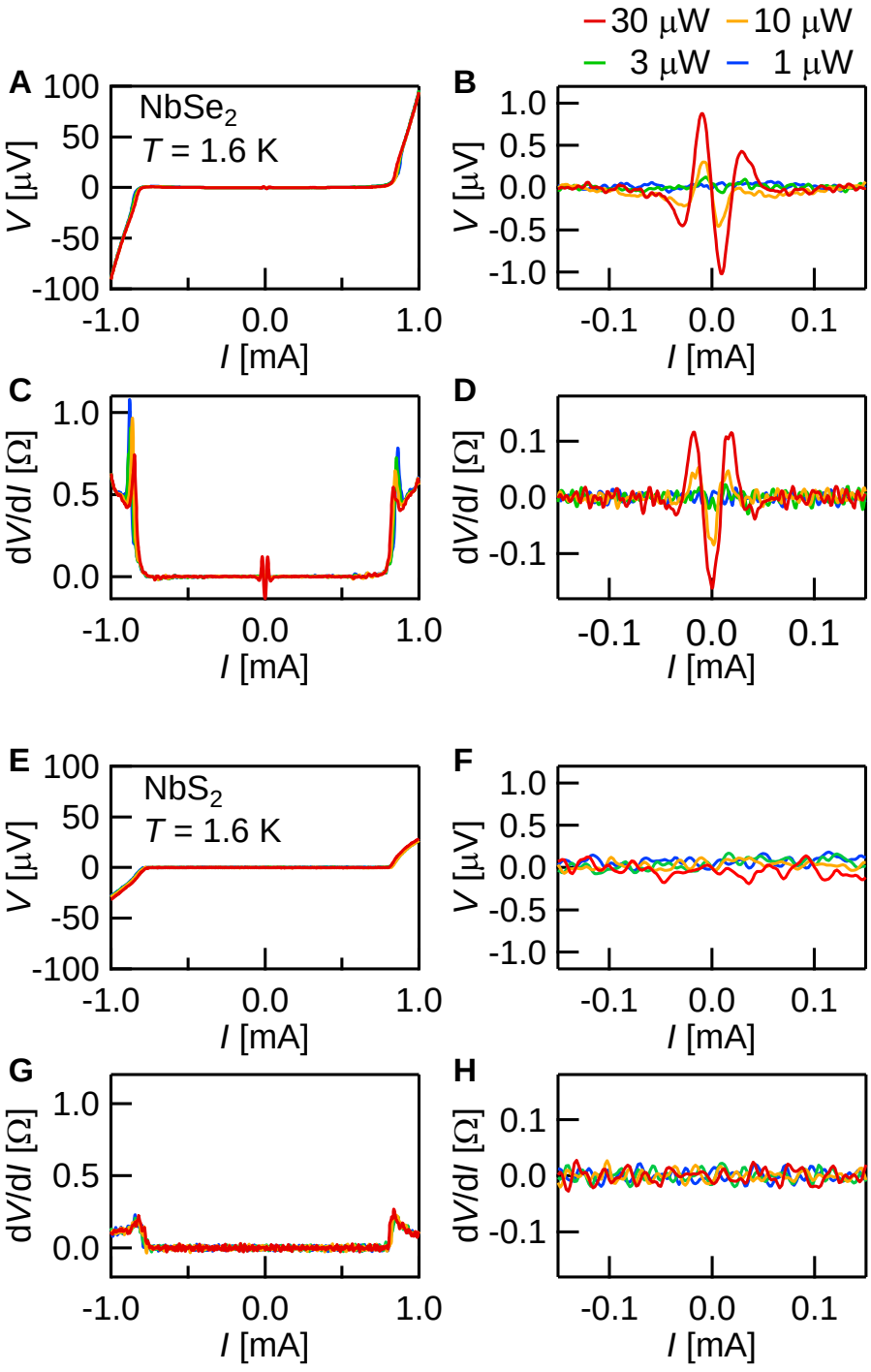

Figure 3.2.1: *I-V* characteristics of $NbSe_2$ (A-D) and NbS_2 (E-H) thin films exposed to SAWs. The *I-V* curves are obtained for four different SAW powers at 1.6 K. The differential resistance is obtained by numerically deviating the *I-V* curve.

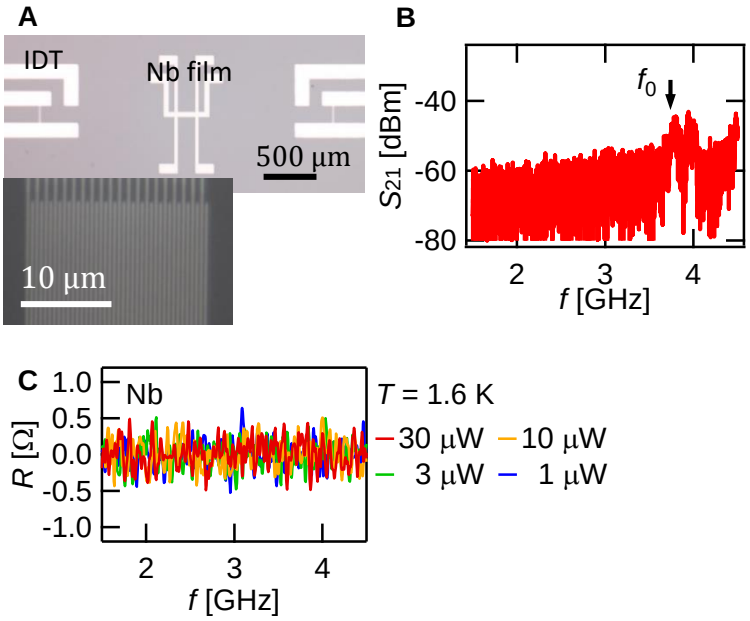

Figure 3.2.2: SAW device fabricated with Nb thin film. (A) Optical microscope image of the device fabricated by the standard sputtering method. The IDTs, which are composed of Nb, are simultaneously fabricated with the Hall bar. (B) S_{21} of the IDTs measured by the network analyzer. The arrow points out the resonance frequency, $f_0 \sim 3.7$ GHz, of the IDTs. The small difference of the resonance frequency between the two IDTs would result in the double peak structure. (C) The resistance of the Nb device as a function of the SAW frequency f. The resistance is measured with four SAW powers at 1.6 K.

resistance emerges when $|I| < 15$ μA or $20 < |I| < 30$ μA. At $T = 1.6$ K and the SAW power of 30 μW, the resistance of the $NbSe_2$ device is about -0.16 Ω, comparable to that of the normal state.

Control experiments are performed using NbS_2 thin films (Figs. 3.2.1E-H). Although I_C is almost the same as the $NbSe_2$ devices, the NbS_2 device does not show such a negative differential resistance in the vicinity of zero bias current. The crystal structure of NbS_2 is the same as that of $NbSe_2$ except for the lattice constant. The Fermi surface is also similar and the transition temperature is com-

parable. A distinct difference between them is the CDW phase. Unlike the case of $NbSe_2$, the CDW phase does not exist in NbS_2. This fact suggests the relevance of the CDW phase for the negative resistance.

Furthermore, we have also conducted control experiments with Nb thin film as a typical conventional superconductor (Fig. 3.2.2). The Hall bar of Nb is fabricated by the standard *dc* sputtering method. Although the Hall bar has a wider and longer shape than the $NbSe_2$ device due to the technical reason, the thickness of the Hall bar is 30 nm which is comparable to the layered material devices. The negative resistance is not observed in the Nb device exposed to the SAWs. This result supports the above consideration.

3.2.2 Temperature and magnetic field dependencies

The negative resistance is further investigated by measuring the temperature and magnetic field dependencies. Figures 3.2.3A and 3.2.3B show the resistances of $NbSe_2$ and NbS_2 devices obtained by the *ac* lock-in technique as a function of temperature. The results show that the differential resistance $\mathrm{d}V/\mathrm{d}I$ obtained from the *dc I-V* curve is equivalent to the resistance measured by the *ac* technique. The amplitude of the negative resistance decreases with increasing temperature. The superconducting transition temperature T_C is independent to the power of SAW. On the other hand, the resistance of the NbS_2 device is zero up to T_C.

Figures 3.2.3C and 3.2.3D show the differential resistances, obtained by numerically differentiating the *I-V* curve, under the SAW irradiation with two different *rf* powers, 1 μW and 30 μW, respectively. As in the case of R measured with the *ac* Lock-in technique shown in Fig 3.2.3A, the numerically obtained $\mathrm{d}V/\mathrm{d}I$

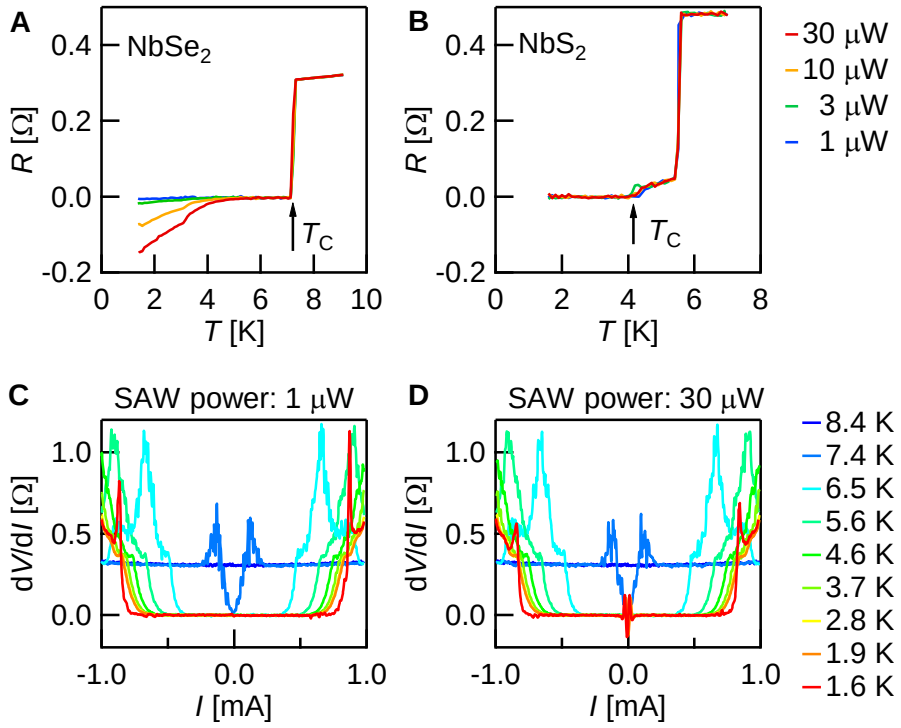

Figure 3.2.3: Temperature dependences of R of (A) the $NbSe_2$ device and (B) the NbS_2 device with different SAW powers. The arrows show the superconducting transition temperature T_C. The differential resistance dV/dI of the $NbSe_2$ device under two different SAW powers, (C) 1 μW and (D) 30 μW, at several temperatures. The differential resistance dV/dI is obtained by numerically differentiating the I-V curve.

curves also show a negative value only for the SAW power of 30 μW. The dV/dI curves near I_C are almost independent of the SAW power at any temperature. With increasing temperature, the critical current I_C decreases as can be expected for a conventional superconductor.

Figures 3.2.4A and 3.2.4B show the resistances of the $NbSe_2$ device and the NbS_2 device as a function of the magnetic field measured at $T = 1.6$ K and under four different SAW powers. It is obvious that the magnetic field strongly suppresses the negative resistance. This suppression can also be seen in the I-V curve

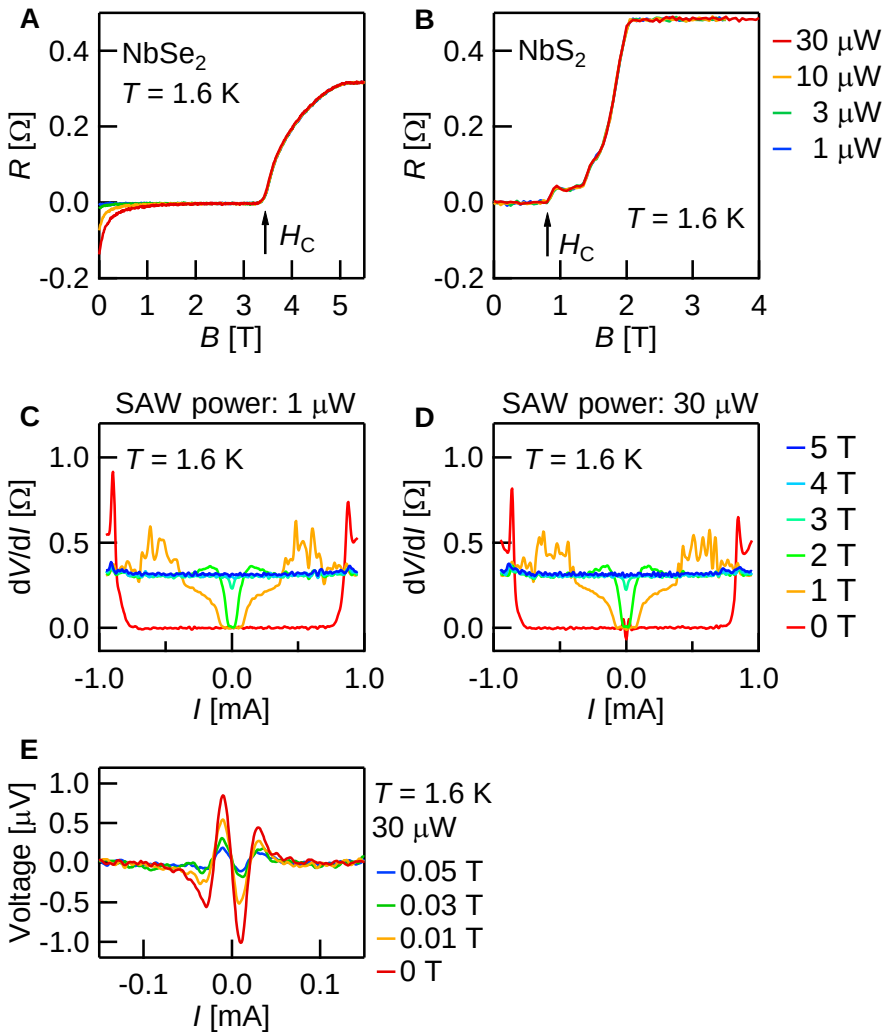

Figure 3.2.4: The magnetic field dependence of R obtained with (A) the $NbSe_2$ device and (B) the NbS_2 device at $T = 1.6$ K. The arrows indicate the critical fields H_C. The dV/dI vs I curves of the $NbSe_2$ are plotted at several different magnetic fields under the SAW power of (C) 1 μW and (D) 30 μW at 1.6 K. (E) The I-V curve exposed to the SAW power of 30 μW at $T = 1.6$ K at small magnetic fields (0$\sim$0.05 T).

(Fig. 3.2.4C-E), where the critical current is not affected by the SAW irradiations. The finite voltage induced by the SAW decreases with increasing the magnetic field (Fig. 3.2.4E). The period of the voltage oscillation is not modulated by the magnetic field. Because $NbSe_2$ is a type-II superconductor, the vortex flow [8] can be a possible origin of the negative resistance. A vortex flows in the vertical directions to the current and also to the magnetic flux because of the Lorentz force. The moving vortex generates an induced electromotive force in the current direction, resulting in a *dc* voltage. However, the vortex flow should predominately affect the critical current regime [154, 155]. This fact and also the strong suppression of the negative resistance by the magnetic field prove that the negative resistance is not caused by the vortex flow.

3.2.3 Frequency dependence

Figure 3.2.5 shows the resistance of the $NbSe_2$ device exposed to the SAW as a function of the *rf* frequency applied to the IDTs. When the SAW power is smaller than 1 μW, the resistance is zero in the investigated frequency range ($1 < f < 5$ GHz). When the SAW power is larger than 3 μW, a sharp dip, namely negative resistance, starts to appear at the resonance frequency of IDTs, f_0. With increasing the power, the dip gets deeper. The result clearly shows that the negative resistance is induced by the SAW. The complicated pattern around the dip also emerges with increasing the SAW power. This could be caused by the nonlinearly-induced phonons [156, 157] or the crosstalk between the IDTs and the electrodes to measure the resistance [50].

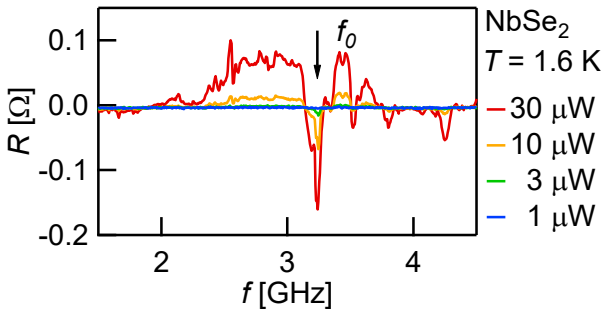

Figure 3.2.5: The resistance of the $NbSe_2$ device as a function of the *rf* frequency applied to the IDTs. The resistance is measured for each power of the microwave at 1.6 K. The arrow indicates the resonance frequency of the IDTs.

3.2.4 Power dependence

Figure 3.2.6 shows the resistance of the $NbSe_2$ device as a function of the SAW power. The resistance is zero up to 1 μW and start to decrease at 3 μW. The amplitude of the negative resistance becomes larger with increasing the SAW power and saturates at -0.15 Ω when the power reaches 25 μW.

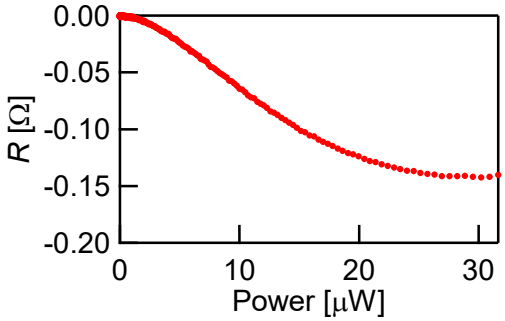

Figure 3.2.6: The resistance of the $NbSe_2$ device measured at $T = 1.6$ K as a function of the SAW power.

3.2.5 Reproducibility of the data

In order to check the reproducibility of the negative resistance, we have confirmed the above tendencies for four different $NbSe_2$ and two different NbS_2 devices from different batches.

Figures 3.2.7A and 3.2.7C show optical microscope images of other two NbSe2 thin film devices where the IDTs are designed in the vicinity of $NbSe_2$ (A) and far from $NbSe_2$ (C). The thicknesses of the $NbSe_2$ flakes are $20 \sim 30$ nm. We measured I-V curves of the two devices at $T = 1.6$ K as shown in Figs. 3.2.7B and 3.2.7D. For both devices, the slopes of the I-V curves are negative, resulting in negative resistances ($-0.10\ \Omega$ and $-0.20\ \Omega$ for the device (A) and the device (C), respectively). We note that the critical current of the device (C) is about 1 mA, while the critical current of the device (A) is about 0.05 mA, which is one order smaller than those of the devices in the main result and shown in (C).

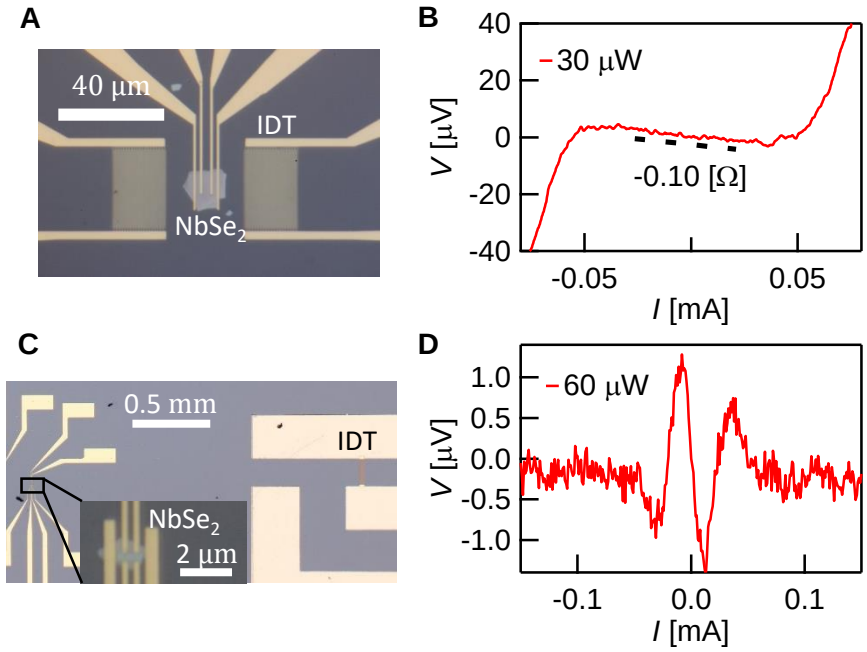

Figure 3.2.7: Reproducibility of negative resistance in other $NbSe_2$ devices. (A, C) Optical microscope images of other two $NbSe_2$ thin film devices where the IDTs are prepared in the vicinity of $NbSe_2$ (A) and far from $NbSe_2$ (C). (B, D) I-V curves measured at T = 1.6 K with the two devices shown in (A) and (C). Only for the device (C), we used two times larger SAW power than that for other devices.

3.3 Short summary

Here, we summarize the experimental results. We have demonstrated a negative resistance in the superconducting gap of $NbSe_2$ thin film on the $LiNbO_3$ substrate induced by the SAW irradiation. The negative resistance appears in the low temperature regime below T_C and its amplitude decreases with increasing temperature. We did not observe any modulation in the *I*-*V* curve above the T_C. These facts reveal that the superconductivity is necessary to induce the negative resistance. The strong suppression of the negative resistance by the magnetic field also indicates the importance of the superconductivity. This suppression proves that the negative resistance is not caused by the vortex flow, which was considered as a possible origin of the negative resistance.

The frequency dependence and the power dependence of the negative resistance reveal that the SAW plays an important role. The negative resistance starts to appear at the resonance frequency of IDTs, f_0, when the SAW power is larger than 3 μW. If the negative resistance is dominated by other effects such as the crosstalk between the IDTs and the electrodes to measure the resistance, the resonance frequency $f_0 \sim 3.2$GHz would not be the characteristic frequency in the frequency dependence.

Control experiments are also performed using NbS_2 thin film devices and a Nb thin film device. In these devices, the negative resistance is not observed. Especially, $NbSe_2$ and NbS_2 have almost the same electronic properties, but the distinct difference between them is the CDW phase. This fact suggests the relevance of the CDW phase for the negative resistance.

Now, we can conclude that it is reasonable to attribute the negative resistance

to cooperative interactions between the superconducting state and the CDW modulated by the SAW. In the next chapter, we will discuss the mechanism of the negative resistance from the theoretical point of view.

Chapter 4

Theoretical descriptions

In this chapter, we discuss our experimental results from the theoretical viewpoint [17]. In Sec. 4.1, we consider the negative resistance in terms of the thermodynamics. In Sec. 4.2, we discuss a Josephson junction shunted by a CDW pass assuming a uniform CDW. In fact, this model does not realize the negative resistance. Finally, in Sec. 4.3, we introduce a soliton model which assumes a non-uniform CDW.

4.1 Negative resistance

In this section, we discuss the negative resistance observed in our experiments. The *dc* electrical resistance is a fundamental property of materials. In a thermal equilibrium state, the linear response resistance cannot be negative because a current flow creates entropy via Joule heating and the entropy production rate must be non-negative as shown in Fig. 4.1.1. An electron flows in the opposite direction to the current bias. The electron loses its energy due to the inelastic scattering by phonons. The obtained phonon energy is relaxed into the thermal bath and this

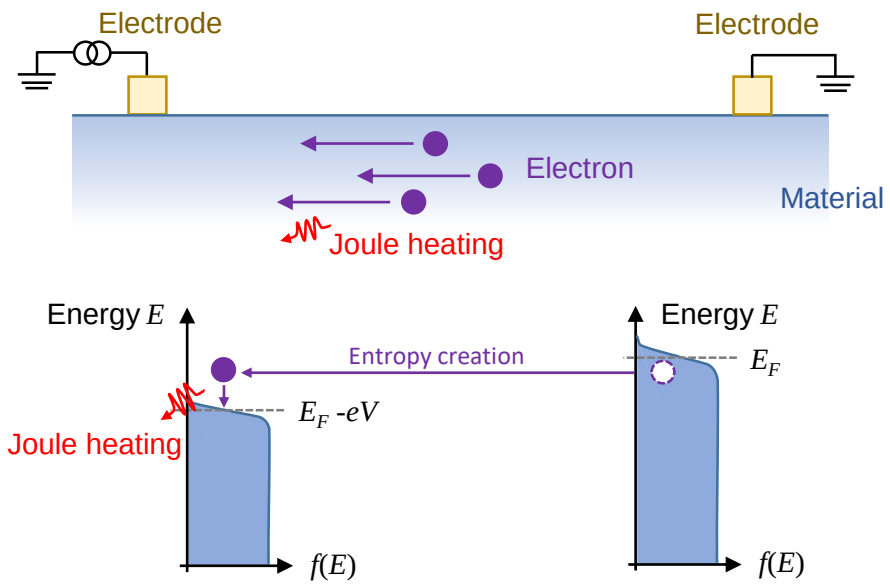

Figure 4.1.1: Schematic images of Joule heating. The motion of the electrons is described in the top figure. The corresponding distribution function $f(E)$ is described in the bottom figure.

result in the Joule heating. In terms of the distribution function $f(E)$ of electrons, the difference of the Fermi energy between the two electrodes is $-eV$, where V is the voltage drop. During this process, electrons with $E > E_{\mathrm{F}}$ and electrons with $E < E_{\mathrm{F}}$ are mixed. Consequently, the current flow produces a non-negative entropy.

Beyond the equilibrium and linear response regime, electronic transport properties can dramatically be changed. A negative absolute resistance state, which is rarely realized, is possible away from the thermal equilibrium because the negative entropy which is proportional to $RI^2 < 0$ term can be compensated by the entropy production.

The negative absolute resistance was discussed for example in 2D electron system (2DES) irradiated by microwaves [4]. The microwave-induced zero re-

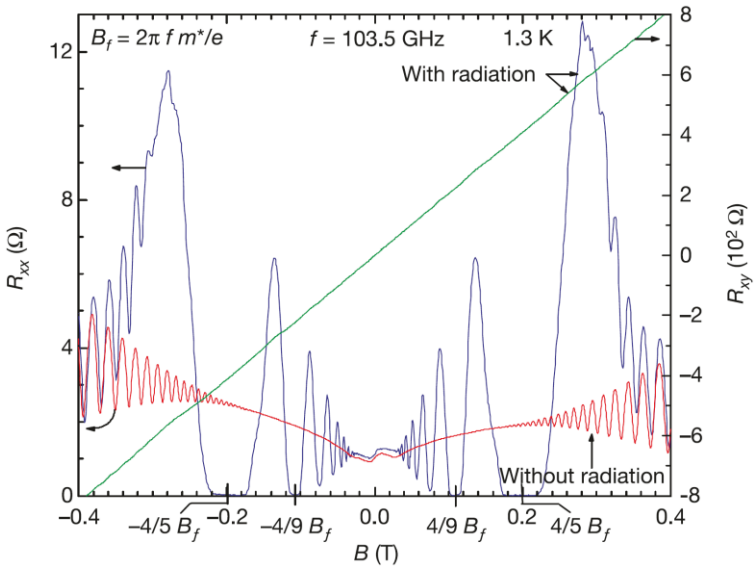

Figure 4.1.2: The Hall effect and the magnetoresistance in a high-mobility 2DES, with and without microwave ($f = 103.5$ GHz) irradiation. Reprinted by permission from Springer Nature Customer Service Centre GmbH: [4].

sistance was observed in a 2DES formed at GaAs/AlGaAs heterojunction [3–6]. A typical Shubnikov-de Haas oscillation was observed in magnetoresistance, but by applying microwaves with a frequency of 103.5 GHz corresponding to two adjacent Landau levels, the magnetoresistance dramatically decreased and finally became zero. This nonequilibrium phenomenon occurs when the microwave frequency coincides with the Landau level splitting energy in the 2DES in a perpendicular magnetic field [3, 6]. In that case, however, the resistance does not take a negative value because the negative resistance state is energetically unstable in normal conductors where Ohm's law governs [3, 7].

In a superconducting state where the resistance is zero up to the critical current, the Ohm's law is not valid anymore but the London equation is used to explain the electrodynamic properties [8]. When microwaves are irradiated to

superconducting junctions, voltage jumps can be observed in the *I*-*V* curve [8], that is known as the ac Josephson effect. In this case, the resistance is still zero (or slightly positive). A negative resistance was observed in a Josephson junction where an *ac* current with a frequency of the GHz range is exposed [158]. In the Josephson junction, the tilt of a washboard type potential is modulated by the microwave current, which can induce a negative resistance at zero bias voltage (see Fig. 1.1.2). However, there are few reports about the negative resistance in Josephson junction and it is still under debate.

We observed the negative resistance in the atomically thin superconducting device irradiated by the SAW. The SAW induces the time-periodical potential, and the power of the SAW is injected into the superconducting thin film. Therefore, the resistance can take a negative value. In general, a time-periodical system can be described as a Floquet state [159]. We can consider that the non-trivial Floquet state is generated in the superconducting thin film by irradiating the SAW. Such a negative resistance state could be a promising stage to demonstrate Floquet engineering in the superconducting state where quantum systems can be driven by the SAW.

4.2 CDW Josephson model

In this section, we try to explain the negative resistance by using the equivalent circuit. As we mentioned in the previous chapter, the essence of the negative resistance is the coexistence of the superconductivity and the CDW. The simplest model is a parallel circuit of the supercurrent, the CDW, and the quasiparticles (Fig. 4.2.1). To take into account the supercurrent, we employ the description similar to that for the Josephson junction. In the superconducting $NbSe_2$ thin film, there would be the regions where the superconducting order parameter is suppressed, relating to the domain structure of the CDW. We regard the region as the Josephson junction shunted by the CDW and the quasiparticles.

The current and the voltage in the supercurrent pass are described with a phase difference θ_{SC} as follows:

$$I_{\mathrm{SC}} = I_0 \sin\theta_{\mathrm{SC}} \tag{4.1}$$

$$V = \frac{\hbar}{2e}\frac{\mathrm{d}\theta_{\mathrm{SC}}}{\mathrm{d}t}. \tag{4.2}$$

We also assume a homogeneous phase for the CDW state. Then, the current and the voltage are given by the following equations:

$$I_{\mathrm{CDW}} = \frac{e}{\pi}\frac{\mathrm{d}\phi_{\mathrm{CDW}}}{\mathrm{d}t} \tag{4.3}$$

$$V = m\frac{\mathrm{d}^2\phi_{\mathrm{CDW}}}{\mathrm{d}t^2} + \gamma\frac{\mathrm{d}\phi_{\mathrm{CDW}}}{\mathrm{d}t} + V_T \sin\phi_{\mathrm{CDW}}, \tag{4.4}$$

where γ and V_T are the damping constant and the pinning potential, respectively.

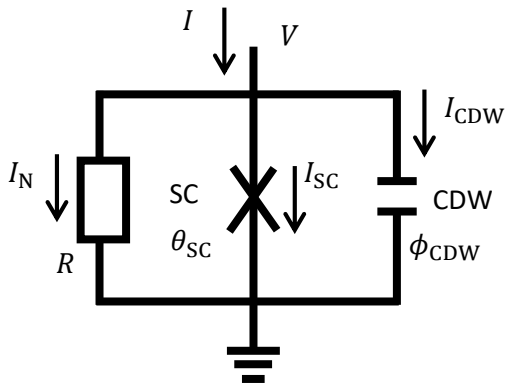

Figure 4.2.1: The equivalent circuit model.

The current-voltage relation for the quasiparticles is given by:

$$V = I_N R. \tag{4.5}$$

The properties of the equivalent circuit can be obtained by solving the simultaneous differential equations.

This equivalent circuit has been used to described the *I*-*V* characteristics of Josephson junction coupled to the CDW state [160–162]. The Josephson junction shunted by the CDW pass is expected to show interesting conduction properties which originate from the non-linearity. Experimentally, however, it is difficult to achieve such a system because of the strong decay of the superconducting order parameter in the CDW material [162]. On the other hand, it is suggested that the model could be used to explain the coexistent systems of the superconductivity and the CDW such as $NbSe_2$ [163]. Because the supercurrent driven by the vector potential is the inductive transport, the Josephson model could describe the essence of the supercurrent. Furthermore, the superconductor can be regarded as

the assemble of the domains whose length scale is the superconducting coherence length ($\sim$ 10 nm for $NbSe_2$). In this sense, the Josephson model with the CDW shunting seems to be reasonable.

Let us consider the case of the strong damping, where the acceleration term is ignored. One of the methods to solve the equivalent circuit model is to transform Eqs. (4.1)-(4.5) to the first-order simultaneous differential equations [164]. Then, the equations can be rewritten as the following dimensionless simultaneous differential equations:

$$\frac{\mathrm{d}\theta_{\mathrm{SC}}}{\mathrm{d}\tau} = I/I_0 - \sin\theta_{\mathrm{SC}} + \frac{e}{\pi\gamma}\frac{V_T}{I_0}\sin\phi_{\mathrm{CDW}} \tag{4.6}$$

$$\frac{\mathrm{d}\phi_{\mathrm{CDW}}}{\mathrm{d}\tau} = (I/I_0 - \sin\theta_{\mathrm{SC}} + \frac{1}{R}\frac{V_T}{I_0}\sin\phi_{\mathrm{CDW}})/\frac{\pi\gamma}{e}\frac{4e^2}{h}, \tag{4.7}$$

where we use the dimensionless time $\tau = t/(\frac{1}{R} + \frac{e}{\pi\gamma})\frac{\hbar}{2eI_0}$. The free parameters are V_T/I_0, R and $\pi\gamma/e$ in a unit of the resistance $h/4e^2$. When the bias current I/I_0 and the initial conditions are given, the time evolutions of the phases can be calculated numerically. Furthermore, the I-V properties can be obtained from the time derivative of θ_{SC}.

Here, we consider the case of *dc* bias current. When $I/I_0 \leq 1$, the fixed points of the deferential equations are obtained from the steady conditions: $\frac{\mathrm{d}\theta_{\mathrm{SC}}}{\mathrm{d}\tau} = 0$ and $\frac{\mathrm{d}\phi_{\mathrm{CDW}}}{\mathrm{d}\tau} = 0$ and the stable fixed point is $(\theta_{\mathrm{SC}}, \phi_{\mathrm{CDW}}) = (\arcsin(I/I_0), 0)$. The time evolutions of the phases converge to the stable fixed point. In the stable fixed state, the bias current flows as the supercurrent which result in the zero resistance. When $I/I_0 > 1$, on the other hand, θ_{SC} rotates with time, resulting in the finite voltage.

We plot $\frac{d\theta_{SC}}{d\tau}$ and $\frac{d\phi_{CDW}}{d\tau}$ in a phase plane as shown in Fig. 4.2.2. The arrows show the angular velocity vector ($\frac{d\theta_{SC}}{d\tau}$, $\frac{d\phi_{CDW}}{d\tau}$) at each point in the ($\theta_{SC}$, ϕ_{CDW}) plane. The length of the vector denotes the absolute value of the angular velocity. The vector can be calculated from Eq. (4.6) and (4.7). Here, we performed the calculation under two different bias currents, $I/I_0 = 0.1$ and $I/I_0 = 1.1$, assuming the free parameter as $\frac{\pi\gamma}{e} = 1$, $\frac{V_T}{I_0} = 2$ and $R = 4$ in a unit of the resistance $h/4e^2$. When the bias current is $I/I_0 = 0.1$, there are one stable fixed point at $(\theta_{SC}, \phi_{CDW}) \sim (0.1, 0)$ and three independent unstable fixed points at $(\theta_{SC}, \phi_{CDW}) \sim (0.1, \pi)$, $(3.0, 0)$ and $(3.0, \pi)$. The phases converge to the fixed point with the time development and thus the voltage becomes zero. On the other hand, there are no fixed point when the bias current is $I/I_0 = 1.1$. Thus θ_{SC} does not converge to a constant value, meaning that a finite *dc* voltage is induced.

This equivalent circuit model gives us the following knowledge:

- The supercurrent pass is in general described by a "nonlinear" inductance, but in the present case, it can be regarded as a "linear" inductance in the small bias current regime.

- The CDW pass is in general described by a "nonlinear" capacitance, but in the present case, it can be regarded as a "linear" capacitance in the small bias voltage regime.

In the CDW phase, the current can be described as $I_{CDW} = \frac{e}{\pi}\frac{d\phi_{CDW}}{dt}$. Thus Eq. (4.4) is equivalent to an equation of RLC series circuit. The acceleration term, the dumping term, and the pinning term correspond to an inductance, a resistance and a capacitance, respectively. This suggests that, as far as we assume the uniform

CDW, the equivalent circuit model including the supercurrent and CDW current cannot explain the negative resistance observed in the zero bias limit. The above discussion also indicates that a non-uniform CDW state should be taken into account.

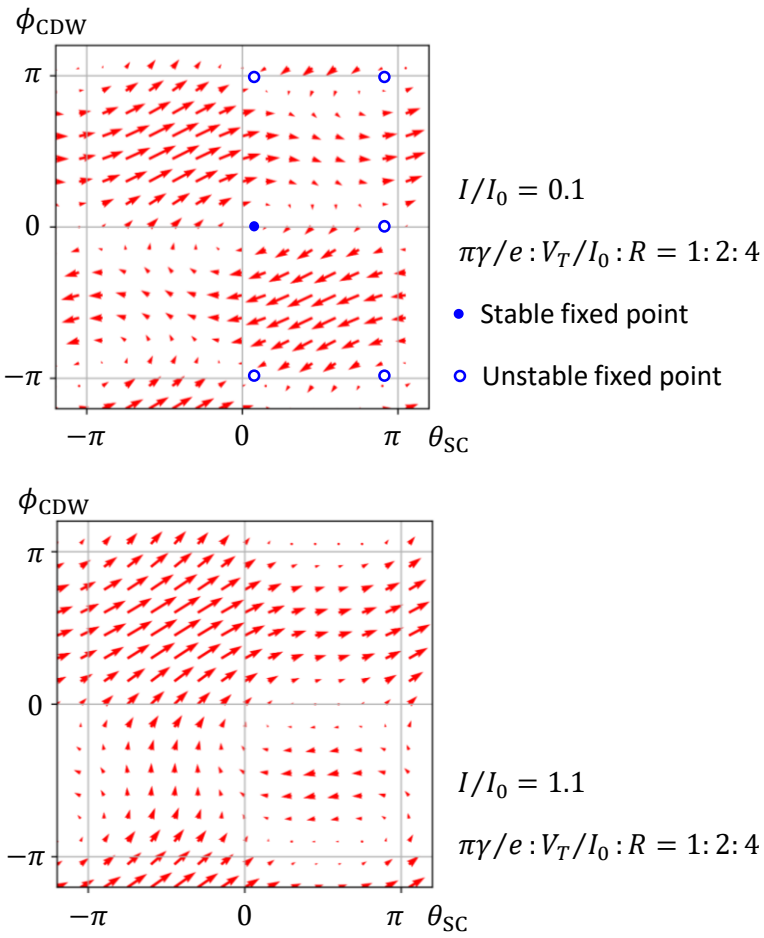

Figure 4.2.2: 2D plots of $\frac{\mathrm{d}\theta_{\mathrm{SC}}}{\mathrm{d}\tau}$ and $\frac{\mathrm{d}\phi_{\mathrm{CDW}}}{\mathrm{d}\tau}$ numerically calculated with two conditions: $I/I_0 = 0.1$ and $I/I_0 = 1.1$, assuming the free parameter as $\frac{\pi\gamma}{e} = 1$, $\frac{V_{\mathrm{T}}}{I_0} = 2$ and $R = 4$ in a unit of the resistance $h/4e^2$. The stable fixed point and the unstable fixed points are described by the blue point and blue circle, respectively.

4.3 Soliton model

4.3.1 Soliton model in CDW and Josephson junction

Since the negative resistance has not been observed in the NbS_2 and Nb devices, it is reasonable to attribute the negative resistance to cooperative interactions between the superconducting state and the CDW modulated by the SAW. One possible scenario is that soliton-antisoliton pairs in the CDW phase [42, 48, 165] are generated by irradiating the SAW and they form local capacitances in the superconducting state. In the CDW phase of $NbSe_2$ (below 33 K), selenium atoms have a periodic modulation that is three times the lattice constant for selenium atoms [122, 137, 149]. When the SAW is irradiated to the $NbSe_2$ device, all the selenium atoms would be shifted from the commensurate position of the CDW and thus the phase ϕ of the CDW order parameter would be modulated over the wavelength of the SAW (= 1 μm), as shown in the upper panel of Fig. 4.3.1. This displacement increases the electrostatic energy as well as the elastic energy. Thus, it is energetically more favorable to nucleate soliton-antisoliton pairs and to induce a phase difference $\Delta\phi$ of 2π in between the soliton-antisoliton pairs [37,42,48,165], as illustrated in the lower panel of Fig. 4.3.1A. Such soliton-antisoliton pairs have been intensively studied in quasi-one-dimensional CDW systems [42,48,165] and also discussed even in 2D CDW compounds [165]. As mentioned in Sec. 2.2, it has been revealed that there are several types of domains with a size of about 10 nm in the equilibrium $NbSe_2$ [137]. This is an additional supportive observation for the soliton-antisoliton pairs in the $NbSe_2$ film. While the CDW opens an energy gap at the Fermi energy, it is not a full-gap state for $NbSe_2$ [166] and thus

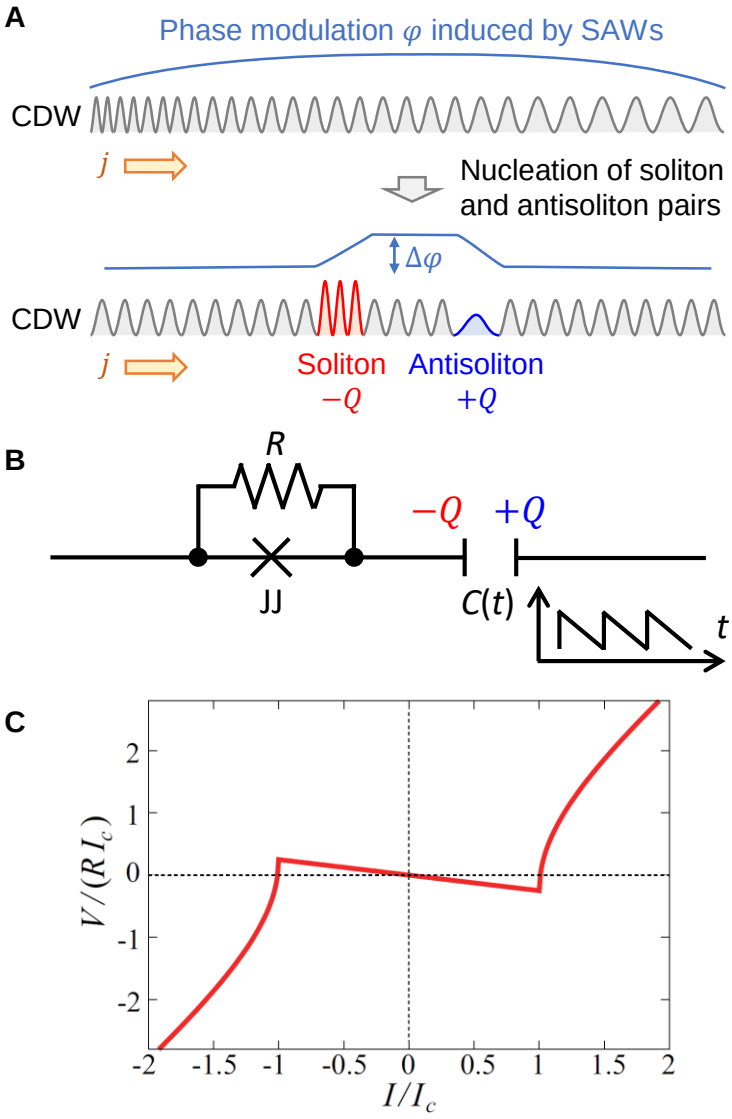

Figure 4.3.1: (A) Schematics of nucleation of soliton and antisoliton pairs. When the SAW is irradiated to the CDW state, the CDW phase ϕ is modulated over the wavelength of the SAW. Instead of modulating over the wavelength, it is more stable to nucleate soliton and antisoliton pairs in the CDW state. In the superconducting state, local charges $(-Q, +Q)$ are accumulated, resulting in a temporal and local capacitance $C(t)$ and a phase difference $\Delta\phi$ of 2π. (B) The circuit model used in the calculation (see next section for more details). We assume a resistively shunted Josephson junction (JJ) which is capaticively coupled via $C(t)$. The change in $C(t)$ is synchronized with the frequency of the SAW. We assume a sawtooth wave function for $C(t)$. (C) A typical I-V curve of the capacitively coupled Josephson junction. The horizontal and vertical axes are normalized by I_C and the product of the resistance R of the normal state and I_C, respectively.

the charge accumulation due to the pair creation is immediately dissolved. On the other hand, the superconducting gap fully opens at the Fermi energy below T_C. Therefore, the charge accumulation is expected to survive longer in the superconducting state so that it can be regarded as a temporal and local capacitance. As for the superconducting part, the shape of the *I*-*V* curve is a typical of overdamped Josephson junction [8]. This fact indicates the existence of weakly coupled superconducting domains in the $NbSe_2$ thin film.

Based on the above experimental facts and ideas, we have developed a capacitively coupled Josephson junction model (see the next sub-section for more details), and calculated an *I*-*V* property of the circuit shown in the upper panel of Fig. 4.3.1B. In this calculation, we assume that the time (t)-dependent local capacitance $C(t)$ between the soliton-antisoliton pairs is modulated by the same frequency as the SAW to have a sawtooth wave as shown in the lower panel of Fig. 4.3.1B. A typical *I*-*V* curve based on this model is displayed in Fig. 4.3.1C (see the next sub-section for derivation). We qualitatively reproduce a negative resistance in the superconducting gap; the negative slope appears at zero current in the superconducting gap.

On the other hand, there is a difference between the experimental result and the theoretical calculation; in most cases (see Sec. 3.2), the negative resistance is realized only in the vicinity of the zero current, while in the present calculation the negative resistance continues up to I_C. Although the dynamics of soliton-antisolition pairs is simply modeled as the time-dependent capacitance in this work, it could be affected by the supercurrent flow via the microscopic interplay between the CDW and superconductivity [167]. Since the effect of such an in-

terplay should become relevant for larger supercurrents, the discrepancy might be resolved by taking it into account in the future work.

4.3.2 Details of the soliton model

We first describe the *I*-*V* characteristic of the superconducting part without the CDW and SAW. Since a hysteretic *I*-*V* curve is not observed near the critical current I_C (Fig. 3.2.1), we use the overdamped approximation and neglect the capacitive part in the standard resistively and capacitively shunted junction model [8]. In this situation, superconducting currents flow through Josephson weak links formed at domains in the thin film $NbSe_2$ device. In the presence of an externally supplied bias current I, the phase difference ϕ_S of the two superconducting domains can be expressed as follows:

$$I = I_C \sin\phi_S + \frac{V_S}{R} \tag{4.8}$$

$$\frac{d\phi_S}{dt} = \frac{2|e|V_S}{\hbar} \tag{4.9}$$

where V_S and R are a voltage across the Josephson junction and a resistance of the normal state, respectively [8].

Next, we consider the CDW part. As we will see below, the SAW can lead to a nontrivial current flow via the CDW. In general, the SAW would affect charge distributions of the system so that the CDW periodic spatial structure may be modulated non-uniformly. An example of such a modulation is locally excited soliton-antisoliton pairs, as detailed in [42, 48, 165]. Since they have electric charges of opposite sign, the soliton-antisoliton pair could be viewed as a capacitance (see

Figs. 4.3.1A and 4.3.1B). In the present CDW state, however, the energy gap is not fully open at the Fermi energy. Even though the soliton-antisoliton pairs are generated, the charge accumulation should be screened immediately by electrons at the Fermi energy. Below the superconducting transition temperature, on the other hand, the energy gap is fully open at the Fermi energy. There are no quasiparticles to screen the generated charges, resulting in a local capacitance as illustrated in Fig. 4.3.1A.

We model the CDW modulation induced by the SAW using a time-dependent capacitance $C(t)$ which should exhibit the same period as the SAW. We assume that the time-dependent $C(t)$ behaves as a sawtooth wave in Fig. 4.3.1B. The electric current I_{CDW} passing through the time-dependent CDW modulation is given by

$$I_{\mathrm{CDW}} = \frac{\mathrm{d}}{\mathrm{d}t}(C(t)V_{\mathrm{CDW}}) = C(t)\frac{\mathrm{d}V_{\mathrm{CDW}}}{\mathrm{d}t} + V_{\mathrm{CDW}}\frac{\mathrm{d}C(t)}{\mathrm{d}t} \tag{4.10}$$

where V_{CDW} is a voltage across the capacitance. It should be noted that the second term on the right-hand side of Eq. (4.10) is peculiar to the present system with the time-dependent capacitance $C(t)$. When $C(t)$ is time-independent as usual, I_{CDW} is zero after a long time average, i.e., $\langle I_{\mathrm{CDW}}\rangle = 0$ and correspondingly, $\langle \mathrm{d}V_{\mathrm{CDW}}/\mathrm{d}t\rangle = 0$ When $C(t)$ has a time-dependent part as in the present case, I_{CDW} can be finite provided that the long-time average of the additional term, $\alpha \equiv \langle \mathrm{d}C(t)/\mathrm{d}t\rangle$, is nonzero. In this case, the voltage across the capacitance is calculated with Eq. (4.10) as $V_{\mathrm{CDW}} = \langle I_{\mathrm{CDW}}\rangle/\alpha$.

We shall combine the superconducting property Eq. (4.8) with the time-dependent CDW sector Eq. (4.10). A minimal model to explain the I-V characteristic would be a resistively shunted Josephson junction coupled by the time-

dependent capacitance $C(t)$ (see Fig. 4.3.1B). We note that one needs a finite energy, the SAW in the present case, to nucleate $C(t)$. Thus, α should be a discontinuous function as a function of the *rf* power. Assuming that α is finite, a nonzero current $\langle I_{\rm CDW}\rangle$ can flow across the capacitance, as already mentioned above. In the presence of an externally supplied bias current I, the voltage drop $V_{\rm CDW}$ across the capacitance is expressed as $V_{\rm CDW} = I/\alpha$. Thus, the set of equations describing the *I*-*V* characteristic in the coexistence of the superconducting and CDW phases irradiated by the SAW are

$$\frac{{\rm d}\phi_{\rm S}}{{\rm d}t} = \frac{2|e|RI_{\rm C}}{\hbar}\left[\frac{I_{\rm C}}{I} - \sin\phi_{\rm S}\right] \tag{4.11}$$

$$V = V_{\rm S} + V_{\rm CDW} = \frac{\hbar}{|e|}\frac{{\rm d}\phi_{\rm S}}{{\rm d}t} + \frac{I}{\alpha} \tag{4.12}$$

where V is a net voltage drop across the time-dependent capacitance and the resistively shunted Josephson junction in series (see Fig. 4.3.1B). Since the time average of the solution of Eq. (4.11) is known to be [8]

$$\frac{\hbar}{2|e|}\langle\frac{{\rm d}\phi_{\rm S}}{{\rm d}t}\rangle = \begin{cases} 0 & (|I| < I_{\rm C}) \\ \frac{RI}{2}\sqrt{1-(I_{\rm C}/I)^2} & (|I| \geq I_{\rm C}) \end{cases} \tag{4.13}$$

Thus, the following equations can be drawn by using Eq. (4.12):

$$\langle V\rangle = \begin{cases} I/\alpha & (|I| < I_{\rm C}) \\ I/\alpha + RI\sqrt{1-(I_{\rm C}/I)^2} & (|I| \geq I_{\rm C}) \end{cases} \tag{4.14}$$

In the case of $\alpha < 0$, the slope of the *I*-*V* curve becomes negative for $|I| < I_{\rm C}$,

pointing to the emergence of the absolute negative resistance. In Fig. 4.3.1C, we show a typical *I*-*V* curve obtained with this model.

Chapter 5

Summary

In this chapter, we summarize this thesis. The purpose of this research is to investigate the electronic properties in atomically thin superconducting films modulated by SAWs. In the following, we summarize what we have conducted and unveiled.

Sample fabrication and SAW techniques

For the purpose mentioned above, we have established the fabrication technique for the integrated device of the SAW and the superconducting thin film. The atomically thin film of $NbSe_2$ can be fabricated by the scotch tape method. The thin film should be handled in a glove box, filled with inert gas, to avoid any degradation. Moreover, due to the pyroelectricity of the $LiNbO_3$ substrate, any baking process should be avoided after the micro-fabrication. The recipe for fabrication provides us the high production yield of the SAW devices. We have also built the experimental setup for low temperature ($\sim$ 1.6 K) transport measurements. The setup includes the high frequency lines for generating the SAW and the *dc* lines for the four terminal measurements. These techniques enable us to investigate the

electronic properties in superconducting thin films modulated by SAWs.

Electrical conduction of superconducting thin film exposed to SAWs

We have observed a negative resistance in the superconducting gap of $NbSe_2$ thin film on the $LiNbO_3$ substrate induced by the SAW irradiation. The negative resistance appears in the low temperature regime below T_C and its amplitude decreases with increasing temperature. Additionally, the magnetic field strongly suppresses the negative resistance. The control experiments, using NbS_2 thin film devices and Nb thin film device, suggest the relevance of the CDW phase for the negative resistance. These results indicate that negative resistance takes place due to the interplay between the superconductivity and the SAW-modulated CDW.

Theoretical descriptions

In order to describe the experimentally observed negative resistance, we have given some theoretical considerations. In general, a negative resistance state at the zero bias limit violates the laws of thermodynamics. By injecting an additional power from outside, however, the resistance can take a negative value. In our case, the power is injected form the SAWs to the electronic system.

Then, we have tried to understand the negative resistance by using a theoretical model based on the RCSJ model. The CDW Josephson model, which assumes the uniform CDW, cannot explain the negative resistance. This result indicates

that we should take into account the non-uniform CDW state, namely the soliton excitations. To describe the soliton excitation, we have introduced the equivalent circuit model composed of the time-dependent capacitance and the resistively shunted Josephson junction in series. This model qualitatively reproduces the experimentally measured negative resistance.

Perspective

In this thesis, we have succeeded in modulating the electronic properties in atomically thin superconducting $NbSe_2$ films by the SAWs. Our results could give rise to a new field of the thin film device. For instance, the negative resistance state could be a promising stage to demonstrate Floquet engineering [159] in the superconducting state where quantum systems can be driven by the SAW.

Bibliography

[1] Leo Esaki. New Phenomenon in Narrow Germanium $p-n$ Junctions. *Phys. Rev.*, **109**:603–604, Jan 1958.

[2] K. Seeger. *Semiconductor Physics - An Introduction, 9th ed.* Springer-Verlag Berlin Heidelberg, 2004.

[3] I. A. Dmitriev, A. D. Mirlin, D. G. Polyakov, and M. A. Zudov. Nonequilibrium phenomena in high Landau levels. *Rev. Mod. Phys.*, **84**:1709–1763, Nov 2012.

[4] R. G. Mani, J. H. Smet, K. von Klitzing, V. Narayanamurti, W. B. Johnson, and V. Umansky. Zero-resistance states induced by electromagnetic-wave excitation in GaAs/AlGaAs heterostructures. *Nature*, **420**:646–650, 2002.

[5] M. A. Zudov, R. R. Du, L. N. Pfeiffer, and K. W. West. Evidence for a New Dissipationless Effect in 2D Electronic Transport. *Phys. Rev. Lett.*, **90**:046807, Jan 2003.

[6] Denis Konstantinov and Kimitoshi Kono. Photon-Induced Vanishing of Magnetoconductance in 2D Electrons on Liquid Helium. *Phys. Rev. Lett.*, **105**:226801, Nov 2010.

[7] A. V. Andreev, I. L. Aleiner, and A. J. Millis. Dynamical Symmetry Breaking as the Origin of the Zero-dc-Resistance State in an ac-Driven System. *Phys. Rev. Lett.*, **91**:056803, Aug 2003.

[8] M. Tinkham. *Introduction to Superconductivity: 2nd ed.* Dover Publications Inc., New York, 2004.

[9] K. S. Novoselov, D. Jiang, F. Schedin, T. J. Booth, V. V. Khotkevich, S. V. Morozov, and A. K. Geim. Two-dimensional atomic crystals. *Proceedings of the National Academy of Sciences*, **102**(30):10451–10453, 2005.

[10] J. T. Ye, Y. J. Zhang, R. Akashi, M. S. Bahramy, R. Arita, and Y. Iwasa. Superconducting Dome in a Gate-Tuned Band Insulator. *Science*, **338**(6111):1193–1196, 2012.

[11] Y. Cao, A. Mishchenko, G. L. Yu, E. Khestanova, A. P. Rooney, E. Prestat, A. V. Kretinin, P. Blake, M. B. Shalom, C. Woods, J. Chapman, G. Balakrishnan, I. V. Grigorieva, K. S. Novoselov, B. A. Piot, M. Potemski, K. Watanabe, T. Taniguchi, S. J. Haigh, A. K. Geim, and R. V. Gorbachev. Quality Heterostructures from Two-Dimensional Crystals Unstable in Air by Their Assembly in Inert Atmosphere. *Nano Letters*, **15**:4914–4921, 2015.

[12] J. Shiogai, Y. Ito, T. Mitsuhashi, T. Nojima, and A. Tsukazaki. Electric-field-induced superconductivity in electrochemically etched ultrathin FeSe filmsonSrTiO$_3$ and MgO. *Nature Physics*, **12**:42–46, 2016.

[13] Ebrahim Sajadi, Tauno Palomaki, Zaiyao Fei, Wenjin Zhao, Philip Bement, Christian Olsen, Silvia Luescher, Xiaodong Xu, Joshua A. Folk, and David H. Cobden. Gate-induced superconductivity in a monolayer topological insulator. *Science*, **362**(6417):922–925, 2018.

[14] Valla Fatemi, Sanfeng Wu, Yuan Cao, Landry Bretheau, Quinn D. Gibson, Kenji Watanabe, Takashi Taniguchi, Robert J. Cava, and Pablo Jarillo-Herrero. Electrically tunable low-density superconductivity in a monolayer topological insulator. *Science*, **362**(6417):926–929, 2018.

[15] E. Preciado, F. J.R. Schülein, A. E. Nguyen, D. Barroso, M. Isarraraz, G. von Son, I-H. Lu, W. Michailow, B. Möller, V. Klee, J. Mann, A. Wixforth, L. Bartels, and H. J. Krenner. Scalable fabrication of a hybrid field-effect and acousto-electric device by direct growth of monolayer $MoS_2/LiNbO_3$. *Nature Communications*, **6**:8593, 2015.

[16] Shijun Zheng, Hao Zhang, Zhihong Feng, Yuanyuan Yu, Rui Zhang, Chongling Sun, Jing Liu, Xuexin Duan, Wei Pang, and Daihua Zhang. Acoustic charge transport induced by the surface acoustic wave in chemical doped graphene. *Applied Physics Letters*, **109**(18):183110, 2016.

[17] M. Yokoi, S. Fujiwara, T. Kawamura, T. Arakawa, K. Aoyama, H. Fukuyama, K. Kobayashi, and Y. Niimi. Negative resistance state in

superconducting $NbSe_2$ induced by surface acoustic waves. *Science Advances*, **6**(34), 2020.

[18] Michio Naito and Shoji Tanaka. Electrical Transport Properties in 2H-NbS_2, -$NbSe_2$, -TaS_2 and -$TaSe_2$. *Journal of the Physical Society of Japan*, **51**(1):219–227, 1982.

[19] H. Kamalingh Onnes. *Leiden Commun.*, **120b, 122b, 124c**, 1911.

[20] Dirk van Delft and Peter Kes. The discovery of superconductivity. *Physics Today*, **63**(9):38–43, 2010.

[21] J. Bardeen, L. N. Cooper, and J. R. Schrieffer. Theory of Superconductivity. *Phys. Rev.*, **108**:1175–1204, Dec 1957.

[22] V.L. Ginzburg and L.D. Landau. *Journal of Experimental and Theoretical Physics (USSR)*, **20**(1064), 1950.

[23] L. P. Gor'kov. *Soviet Physics-JEPT*, **6**(505), 1958.

[24] L. P. Gor'kov. *Soviet Physics-JEPT*, **9**(1364), 1959.

[25] F. London, H. London, and Frederick Alexander Lindemann. The electromagnetic equations of the supraconductor. *Proceedings of the Royal Society of London. Series A - Mathematical and Physical Sciences*, **149**(866):71–88, 1935.

[26] J. Halbritter. On surface resistance of superconductors. *Zeitschrift für Physik*, 266(3):209–217, Jun 1974.

[27] B.D. Josephson. Possible new effects in superconductive tunnelling. *Physics Letters*, **1**(7):251 – 253, 1962.

[28] A. Barone and G. Paternò. *Physics and applications of the Josephson effect*. Wiley, New York, NY, 1982.

[29] R. E. Peierls. *Quantum Theory of Solids*. Oxford Univ. Press, New York, 1955.

[30] Herbert Fröhlich. On the theory of superconductivity: the one-dimensional case. *Proceedings of the Royal Society of London. Series A. Mathematical and Physical Sciences*, **223**(1154):296–305, 1954.

[31] William Fogle and Jerome H. Perlstein. Semiconductor-to-Metal Transition in the Blue Potassium Molybdenum Bronze, $K_{0.30}MoO_3$; Example of a Possible Excitonic Insulator. *Phys. Rev. B*, **6**:1402–1412, Aug 1972.

[32] D. E. Moncton, J. D. Axe, and F. J. DiSalvo. Neutron scattering study of the charge-density wave transitions in 2H-$TaSe_2$ and 2H-$NbSe_2$. *Phys. Rev. B*, **16**:801–819, Jul 1977.

[33] P. Monçeau, N. P. Ong, A. M. Portis, A. Meerschaut, and J. Rouxel. Electric Field Breakdown of Charge-Density-Wave—Induced Anomalies in $NbSe_3$. *Phys. Rev. Lett.*, **37**:602–606, Sep 1976.

[34] Yongchang Ma, Cuimin Lu, Xuewei Wang, Xueli Du, Lijun Li, and Cedomir Petrovic. Field-induced dielectric response saturation in o-TaS_3. *Journal of Physics: Condensed Matter*, **28**(39):395901, aug 2016.

[35] P.W. Anderson, P.A. Lee, and M. Saitoh. Remarks on giant conductivity in TTF-TCNQ. *Solid State Communications*, **13**(5):595 – 598, 1973.

[36] R. C. Lacoe, H. J. Schulz, D. Jérome, K. Bechgaard, and I. Johannsen. Observation of Nonlinear Electrical Transport at the Onset of a Peierls Transition in an Organic Conductor. *Phys. Rev. Lett.*, **55**:2351–2354, Nov 1985.

[37] G. Grüner. *Density Waves in Solids*. Addison-Wesley, Reading, MA, 1994.

[38] P.A. Lee, T.M. Rice, and P.W. Anderson. Conductivity from charge or spin density waves. *Solid State Communications*, **14**(8):703 – 709, 1974.

[39] H. Fukuyama and P. A. Lee. Dynamics of the charge-density wave. I. Impurity pinning in a single chain. *Phys. Rev. B*, **17**:535–541, Jan 1978.

[40] P. A. Lee and T. M. Rice. Electric field depinning of charge density waves. *Phys. Rev. B*, **19**:3970–3980, Apr 1979.

[41] T. C. Jones, Xinlei Wu, C. R. Simpson, J. A. Clayhold, and J. P. McCarten. Pulse-duration memory effect in $NbSe_3$ and comparison with numerical simulations of phase organization. *Phys. Rev. B*, **61**:10066–10075, Apr 2000.

[42] J. H. Miller, A. I. Wijesinghe, Z. Tang, and A. M. Guloy. Correlated Quantum Transport of Density Wave Electrons. *Phys. Rev. Lett.*, **108**:036404, Jan 2012.

[43] E. C. Geil and R. E. Thorne. Spatially Resolved Transient Dynamics of Charge Density Waves in $NbSe_3$. *Phys. Rev. Lett.*, **114**:016404, Jan 2015.

[44] T. Matsuura, J. Hara, K. Inagaki, M. Tsubota, T. Hosokawa, and S. Tanda. Charge density wave soliton liquid. *EPL (Europhysics Letters)*, **109**(2):27005, jan 2015.

[45] N. Manton and Sutcliffe P. *Topological Solitons*. Cambridge University Press, Cambridge, 2004.

[46] Kazumi Maki. Creation of Soliton Pairs by Electric Fields in Charge-Density-Wave Condensates. *Phys. Rev. Lett.*, **39**:46–48, Jul 1977.

[47] I.V. Krive and A.S. Rozhavsky. On the nature of threshold electric field in quasi-one-dimensional commensurate charge-density-waves. *Solid State Communications*, **55**(8):691 – 694, 1985.

[48] J. H. Miller, A. I. Wijesinghe, Z. Tang, and A. M. Guloy. Coherent quantum transport of charge density waves. *Phys. Rev. B*, **87**:115127, Mar 2013.

[49] D. R. Morgan. *Surface Acoustic Wave Filters (Second edition)*. Academic Press, Oxford, UK, 2007.

[50] C. Campbell. *Surface Acoustic Wave Devices and Their Signal Processing Applications*. Academic Press, San Diego, 1989.

[51] Lord Rayleigh. On Waves Propagated along the Plane Surface of an Elastic Solid. *Proceedings of the London Mathematical Society*, **s1-17**(1):4–11, 1885.

[52] K. Aki and P. G. Richards. *Quantitative Seismology (2nd edition)*.

[53] R. M. White and F. W. Voltmer. DIRECT PIEZOELECTRIC COUPLING TO SURFACE ELASTIC WAVES. *Applied Physics Letters*, **7**(12):314–316, 1965.

[54] S. Datta. *Surface acoustic wave devices*. Prentice-Hall, Englewood, NJ, 1986.

[55] A. Wixforth, J. P. Kotthaus, and G. Weimann. Quantum Oscillations in the Surface-Acoustic-Wave Attenuation Caused by a Two-Dimensional Electron System. *Phys. Rev. Lett.*, **56**:2104–2106, May 1986.

[56] A. Wixforth, J. Scriba, M. Wassermeier, J. P. Kotthaus, G. Weimann, and W. Schlapp. Surface acoustic waves on GaAs/$Al_xGa_{1-x}As$ heterostructures. *Phys. Rev. B*, **40**:7874–7887, Oct 1989.

[57] S. Datta. *Electronic Transport in Mesoscopic Systems*. Cambridge University Press, Cambridge, 1997.

[58] V. I. Talyanskii, J. M. Shilton, M. Pepper, C. G. Smith, C. J. B. Ford, E. H. Linfield, D. A. Ritchie, and G. A. C. Jones. Single-electron transport in a one-dimensional channel by high-frequency surface acoustic waves. *Phys. Rev. B*, **56**:15180–15184, Dec 1997.

[59] M. Kataoka, R. J. Schneble, A. L. Thorn, C. H. W. Barnes, C. J. B. Ford, D. Anderson, G. A. C. Jones, I. Farrer, D. A. Ritchie, and M. Pepper. Single-Electron Population and Depopulation of an Isolated Quantum Dot Using a Surface-Acoustic-Wave Pulse. *Phys. Rev. Lett.*, **98**:046801, Jan 2007.

[60] S. Rahman, M. Kataoka, C. H. W. Barnes, and H. P. Langtangen. Numerical investigation of a piezoelectric surface acoustic wave interaction with a one-dimensional channel. *Phys. Rev. B*, **74**:035308, Jul 2006.

[61] M. Kataoka, C. J. B. Ford, C. H. W. Barnes, D. Anderson, G. A. C. Jones, H. E. Beere, D. A. Ritchie, and M. Pepper. The effect of pulse-modulated surface acoustic waves on acoustoelectric current quantization. *Journal of Applied Physics*, **100**(6):063710, 2006.

[62] Christopher Bäuerle, D Christian Glattli, Tristan Meunier, Fabien Portier, Patrice Roche, Preden Roulleau, Shintaro Takada, and Xavier Waintal. Coherent control of single electrons: a review of current progress. *Reports on Progress in Physics*, **81**(5):056503, apr 2018.

[63] S. Hermelin, S. Takada, M. Yamamoto, S. Tarucha, A. D. Wieck, L. Saminadayar, C. Bäuerle, and T. Meunier. Electrons surfing on a sound wave as a platform for quantum optics with flying electrons. *Nature*, **477**:435–438, 2011.

[64] R. P. G. McNeil, M. Kataoka, C. J. B. Ford, C. H. W. Barnes, D. Anderson, G. A. C. Jones, I. Farrer, and D. A. Ritchie. On-demand single-electron transfer between distant quantum dots. *Nature*, **477**:439–442, 2011.

[65] S. Takada, H. Edlbauer, H. V. Lepage, J. Wang, P.-A. Mortemousque, G. Georgiou, Crispin H. W. Barnes, C. J. B. Ford, M. Yuan, P. V. Santos, X. Waintal, A. Ludwig, A. D. Wieck, M. Urdampilleta, T. Meunier, and C. Bäuerle. Sound-driven single-electron transfer in a circuit of coupled quantum rails. *Nature Communications*, **10**:4557, 2019.

[66] W. J. M. Naber, T. Fujisawa, H. W. Liu, and W. G. van der Wiel. Surface-Acoustic-Wave-Induced Transport in a Double Quantum Dot. *Phys. Rev. Lett.*, **96**:136807, Apr 2006.

[67] Yuya Sato, Jason C. H. Chen, Masayuki Hashisaka, Koji Muraki, and Toshimasa Fujisawa. Two-electron double quantum dot coupled to coherent photon and phonon fields. *Phys. Rev. B*, **96**:115416, Sep 2017.

[68] M. V. Gustafsson, T. Aref, A. F. Kockum, M. K. Ekström, G. Johansson, and P. Delsing. Propagating phonons coupled to an artificial atom. *Science*, **346**(6206):207–211, 2014.

[69] T. Aref, P. Delsing, M. K. Ekström, A. F. Kockum, M. V. Gustafsson, G. Johansson, P. J. Leek, E. Magnusson, and R. Manenti. *Quantum Acoustics with Surface Acoustic Waves*, pages 217–244. Springer International Publishing, Cham, 2016.

[70] R. Manenti, A. F. Kockum, A. Patterson, T. Behrle, J. Rahamim, G. Tancredi, F. Nori, and P. J. Leek. Circuit quantum acoustodynamics with surface acoustic waves. *Nature Communications*, **8**:975, 2017.

[71] Bradley A. Moores, Lucas R. Sletten, Jeremie J. Viennot, and K. W. Lehnert. Cavity Quantum Acoustic Device in the Multimode Strong Coupling Regime. *Phys. Rev. Lett.*, **120**:227701, May 2018.

[72] K. J. Satzinger, Y. P. Zhong, H.-S. Chang, G. A. Peairs, A. Bienfait, M.-H. Chou, A. Y. Cleland, C. R. Conner, . Dumur, J. Grebel, I. Gutierrez, B. H. November, R. G. Povey, S. J. Whiteley, D. D. Awschalom, D. I. Schuster, and A. N. Cleland. Quantum control of surface acoustic-wave phonons. *Nature*, **563**:661–665, 2018.

[73] Per Delsing, Andrew N Cleland, Martin J A Schuetz, Johannes Knrzer, Géza Giedke, J Ignacio Cirac, Kartik Srinivasan, Marcelo Wu, Krishna Coimbatore Balram, Christopher Buerle, Tristan Meunier, Christopher J B Ford, Paulo V Santos, Edgar Cerda-Méndez, Hailin Wang, Hubert J Krenner, Emeline D S Nysten, Matthias Weiß, Geoff R Nash, Laura Thevenard, Catherine Gourdon, Pauline Rovillain, Max Marangolo, Jean-Yves Duquesne, Gerhard Fischerauer, Werner Ruile, Alexander Reiner, Ben Paschke, Dmytro Denysenko, Dirk Volkmer, Achim Wixforth, Henrik Bruus, Martin Wiklund, Julien Reboud, Jonathan M Cooper, YongQing Fu, Manuel S Brugger, Florian Rehfeldt, and Christoph Westerhausen. The 2019 surface acoustic waves roadmap. *Journal of Physics D: Applied Physics*, **52**(35):353001, jul 2019.

[74] A. K. Geim and I. V. Grigorieva. Van der Waals heterostructures. *Nature*, **499**:419–425, 2013.

[75] A Hernández-Mínguez, Y-T Liou, and P V Santos. Interaction of surface acoustic waves with electronic excitations in graphene. *Journal of Physics D: Applied Physics*, **51**(38):383001, aug 2018.

[76] T. Poole and G. R. Nash. Acoustoelectric Current in Graphene Nanoribbons. *Scientific Reports*, **7**:1767, 2017.

[77] Tongyun Huang, Peng Han, Xinke Wang, Jiasheng Ye, Wenfeng Sun, Shengfei Feng, and Yan Zhang. Theoretical study on dynamic acoustic modulation of free carriers, excitons, and trions in 2D MoS_2 flake. *Journal of Physics D: Applied Physics*, **50**(11):114005, feb 2017.

[78] Amgad R. Rezk, Benjamin Carey, Adam F. Chrimes, Desmond W. M. Lau, Brant C. Gibson, Changxi Zheng, Michael S. Fuhrer, Leslie Y. Yeo, and Kourosh Kalantar-zadeh. Acoustically-Driven Trion and Exciton Modulation in Piezoelectric Two-Dimensional MoS_2. *Nano Letters*, **16**(2):849–855, 2016. PMID: 26729449.

[79] Shijun Zheng, Enxiu Wu, Zhihong Feng, Rao Zhang, Yuan Xie, Yuanyuan Yu, Rui Zhang, Quanning Li, Jing Liu, Wei Pang, Hao Zhang, and Daihua Zhang. Acoustically enhanced photodetection by a black phosphorusMoS_2 van der Waals heterojunction pn diode. *Nanoscale*, **10**:10148–10153, 2018.

[80] S. Zheng, E. Wu, and H. Zhang. Anomalous Acoustoelectric Currents in Few-Layer Black Phosphorus Nanocrystals. *IEEE Transactions on Nanotechnology*, **17**(3):590–595, May 2018.

[81] Lokeshwar Bandhu and Geoffrey R. Nash. Controlling the properties of surface acoustic waves using graphene. *Nano Research*, **9**(3):685–691, Mar 2016.

[82] J Liang, B-H Liu, H-X Zhang, H Zhang, M-L Zhang, D-H Zhang, and W Pang. Monolithic acoustic graphene transistors based on lithium niobate thin film. *Journal of Physics D: Applied Physics*, **51**(20):204001, apr 2018.

[83] F. Akao. Attenuation of elastic surface waves in thin film superconducting Pb and In at 316 MHz. *Physics Letters A*, **30**(7):409 – 410, 1969.

[84] E. Krtzig, K. Walther, and W. Schilz. Investigation of superconducting phase transitions in Pb-films with acoustic surface waves. *Physics Letters A*, **30**(7):411 – 412, 1969.

[85] E. Krätzig. Ultrasonic-Surface-Wave Attenuation of Gapless Superconductors. *Phys. Rev. B*, **7**:119–129, Jan 1973.

[86] W. H. Zachariasen. Skr. Norske Vidensk Akad. (No. 4) , 1928.

[87] B. T. Matthias and J. P. Remeika. Ferroelectricity in the Ilmenite Structure. *Phys. Rev.*, **76**:1886–1887, Dec 1949.

[88] ALBERT A. BALLMAN. Growth of Piezoelectric and Ferroelectric Materials by the CzochraIski Technique. *Journal of the American Ceramic Society*, **48**(2):112–113, 1965.

[89] K. Nassau, H.J. Levinstein, and G.M. Loiacono. Ferroelectric lithium niobate. 1. Growth, domain structure, dislocations and etching. *Journal of Physics and Chemistry of Solids*, **27**(6):983 – 988, 1966.

[90] K. Nassau, H.J. Levinstein, and G.M. Loiacono. Ferroelectric lithium niobate. 2. Preparation of single domain crystals. *Journal of Physics and Chemistry of Solids*, **27**(6):989 – 996, 1966.

[91] S.C. Abrahams, J.M. Reddy, and J.L. Bernstein. Ferroelectric lithium niobate. 3. Single crystal X-ray diffraction study at 24 ° C. *Journal of Physics and Chemistry of Solids*, **27**(6):997 – 1012, 1966.

[92] S.C. Abrahams, W.C. Hamilton, and J.M. Reddy. Ferroelectric lithium niobate. 4. Single crystal neutron diffraction study at 24 ° C. *Journal of Physics and Chemistry of Solids*, **27**(6):1013 – 1018, 1966.

[93] S.C. Abrahams, H.J. Levinstein, and J.M. Reddy. Ferroelectric lithium niobate. 5. Polycrystal X-ray diffraction study between 24 ° C and 1200 ° C. *Journal of Physics and Chemistry of Solids*, **27**(6):1019 – 1026, 1966.

[94] Kazuhiko Yamanouchi and Kimio Shibayama. Propagation and Amplification of Rayleigh Waves and Piezoelectric Leaky Surface Waves in $LiNbO_3$. *Journal of Applied Physics*, **43**(3):856–862, 1972.

[95] Koichi Momma and Fujio Izumi. *VESTA3* for three-dimensional visualization of crystal, volumetric and morphology data. *Journal of Applied Crystallography*, **44**(6):1272–1276, Dec 2011.

[96] R. H. Tancrell and M. G. Holland. Acoustic surface wave filters. *Proceedings of the IEEE*, 59(3):393–409, March 1971.

[97] K. S. Novoselov, A. K. Geim, S. V. Morozov, D. Jiang, Y. Zhang, S. V. Dubonos, I. V. Grigorieva, and A. A. Firsov. Electric Field Effect in Atomically Thin Carbon Films. *Science*, **306**(5696):666–669, 2004.

[98] K. S. Novoselov, V. I. Fal'ko, L. Colombo, P. R. Gellert, M. G. Schwab, and K. Kim. A roadmap for graphene. *Nature*, **490**:192–200, 2012.

[99] B. Radisavljevic, A. Radenovic, J. Brivio, V. Giacometti, and A. Kis. Single-layer MoS_2 transistors. *Nature Nanotechnology*, **6**:147–150, 2011.

[100] K. F. Mak, K. L. McGill, J. Park, and P. L. McEuen. The valley Hall effect in MoS_2 transistors. *Science*, **344**(6191):1489–1492, 2014.

[101] J. M. Lu, O. Zheliuk, I. Leermakers, N. F. Q. Yuan, U. Zeitler, K. T. Law, and J. T. Ye. Evidence for two-dimensional Ising superconductivity in gated MoS_2. *Science*, **350**(6266):1353–1357, 2015.

[102] M. Yoshida, J. Ye, T. Nishizaki, N. Kobayashi, and Y. Iwasa. Electrostatic and electrochemical tuning of superconductivity in two-dimensional $-NbSe_2$ crystals. *Applied Physics Letters*, **108**(20):202602, 2016.

[103] X. Xi, L. Zhao, Z. Wang, H. Berger, L. Forró, J. Shan, and Kin Fai Mak. Strongly enhanced charge-density-wave order in monolayer $NbSe_2$. *Nature Nanotechnology*, **10**:765–769, 2015.

[104] X. Xi, Z. Wang, W. Zhao, J.-H. Park, K. T. Law, H. Berger, L. Forró, J. Shan, and K. F. Mak. Ising pairing in superconducting $NbSe_2$ atomiclayers. *Nature Physics*, **12**:139–143, 2016.

[105] M. Yankowitz, J. Xue, D. Cormode, J. D. Sanchez-Yamagishi, K. Watanabe, T. Taniguchi, P. Jarillo-Herrero, P. Jacquod, and B. J. LeRoy. Emergence of superlattice Dirac points in graphene on hexagonal boron nitride. *Nature Physics*, **8**:382–386, 2012.

[106] L. A. Ponomarenko, R. V. Gorbachev, G. L. Yu, D. C. Elias, R. Jalil, A. A. Patel, A. Mishchenko, A. S. Mayorov, C. R. Woods, J. R. Wallbank, M. Mucha-Kruczynski, B. A. Piot, M. Potemski, I. V. Grigorieva, K. S. Novoselov, F. Guinea, V. I. Fal ' ko, and A. K. Geim. Cloning of Dirac fermions in graphene superlattices. *Nature*, **497**:594–597, 2013.

[107] C. R. Dean, L. Wang, P. Maher, C. Forsythe, F. Ghahari, Y. Gao, J. Katoch, M. Ishigami, P. Moon, M. Koshino, T. Taniguchi, K. Watanabe, K. L. Shepard, J. Hone, and P. Kim. Hofstadter's butterfly and the fractal quantum Hall effect in moir superlattices. *Nature*, **497**:598–602, 2013.

[108] Xiaoxiang Xi, Helmuth Berger, László Forró, Jie Shan, and Kin Fai Mak. Gate Tuning of Electronic Phase Transitions in Two-Dimensional $NbSe_2$. *Phys. Rev. Lett.*, **117**:106801, Aug 2016.

[109] X. Wang, L.X. You, D.K. Liu, C.T. Lin, X.M. Xie, and M.H. Jiang. Thin-film-like BSCCO single crystals made by mechanical exfoliation. *Physica C: Superconductivity*, **474**:13 – 17, 2012.

[110] A. Jindal, D. A. Jangade, N. Kumar, J. Vaidya, I. Das, R. Bapat, J. Parmar, B. A. Chalke, A. Thamizhavel, and M. M. Deshmukh. Growth of high-quality $Bi_2Sr_2CaCu_2O_{8+\delta}$ whiskers and electrical properties of resulting exfoliated flakes. *Scientific Reports*, **7**:3295, 2017.

[111] Shota Suzuki, Hiroki Taniguchi, Tsukasa Kawakami, Maxen Cosset-Cheneau, Tomonori Arakawa, Shigeki Miyasaka, Setsuko Tajima, Yasuhiro Niimi, and Kensuke Kobayashi. Electrical contacts to thin layers of $Bi_2Sr_2CaCu_2O_{8+\delta}$. *Applied Physics Express*, **11**(5):053201, apr 2018.

[112] S. Y. Frank Zhao, Nicola Poccia, Margaret G. Panetta, Cyndia Yu, Jedediah W. Johnson, Hyobin Yoo, Ruidan Zhong, G. D. Gu, Kenji Watanabe, Takashi Taniguchi, Svetlana V. Postolova, Valerii M. Vinokur, and Philip Kim. Sign-Reversing Hall Effect in Atomically Thin High-Temperature $Bi_{2.1}Sr_{1.9}CaCu_{2.0}O_{8+\delta}$ Superconductors. *Phys. Rev. Lett.*, **122**:247001, Jun 2019.

[113] C. Gong, L. Li, Z. Li, H. Ji, A. Stern, Xia Y., T. Cao, W. Bao, C. Wang, Y. Wang, Z. Q. Qiu, R. J. Cava, S. G. Louie, J. Xia, and X. Zhang. Discovery of intrinsic ferromagnetism in two-dimensional van der Waals crystals. *Nature*, **546**:265–269, 2017.

[114] B. Huang, G. Clark, E. Navarro-Moratalla, D. R. Klein, R. Cheng, K. L. Seyler, D. Zhong, E. Schmidgall, M. A. McGuire, D. H. Cobden, W. Yao, D. Xiao, P. Jarillo-Herrero, and X. Xu. Layer-dependent ferromagnetism in a van der Waals crystal down to the monolayer limit. *Nature*, **546**:270–273, 2017.

[115] Y. Deng, Y. Yu, Y. Song, J. Zhang, N. Z. Wang, Z. Sun, , Y. Yi, Y. Z. Wu, S. Wu, J. Zhu, J. Wang, X. H. Chen, and Y. Zhang. Gate-tunable room-temperature ferromagnetism in two-dimensional Fe_3GeTe_2. *Nature*, **563**:94–99, 2018.

[116] K. Motizuki. *Structural Phase Transitions in Layered Transition Metal Compounds*. Reidel, Dordrecht, Netherlands, 1986.

[117] Agnieszka Kuc and Thomas Heine. The electronic structure calculations of two-dimensional transition-metal dichalcogenides in the presence of external electric and magnetic fields. *Chem. Soc. Rev.*, **44**:2603–2614, 2015.

[118] C. H. Ahn, A. Bhattacharya, M. Di Ventra, J. N. Eckstein, C. Daniel Frisbie, M. E. Gershenson, A. M. Goldman, I. H. Inoue, J. Mannhart, Andrew J. Millis, Alberto F. Morpurgo, Douglas Natelson, and Jean-Marc Triscone. Electrostatic modification of novel materials. *Rev. Mod. Phys.*, **78**:1185–1212, Nov 2006.

[119] K. Ueno, S. Nakamura, H. Shimotani, A. Ohtomo, N. Kimura, T. Nojima, H. Aoki, Y. Iwasa, and M. Kawasaki. Electric-field-induced superconductivity in an insulator. *Nature Materials*, **7**:855–858, 2008.

[120] A. T. Bollinger, G. Dubuis, J. Yoon, D. Pavuna, J. Misewich, and I. Božović. Superconductorinsulator transition in $La_{2-x}Sr_xCuO_4$ at the pair quantum resistance. *Nature*, **472**:458–460, 2011.

[121] Trevor A. Petach, Menyoung Lee, Ryan C. Davis, Apurva Mehta, and David Goldhaber-Gordon. Mechanism for the large conductance modulation in electrolyte-gated thin gold films. *Phys. Rev. B*, **90**:081108, Aug 2014.

[122] M. M. Ugeda, Aaron J. Bradley, Y. Zhang, S. Onishi, Y. Chen, W. Ruan, C. Ojeda-Aristizabal, H. Ryu, M. T. Edmonds, H.-Z. Tsai, A. Riss, S.-K. Mo, D. Lee, A. Zettl, Z. Hussain, Z.-X. Shen, and M. F. Crommie. Characterization of collective ground states in single-layer $NbSe_2$. *Nature Phisics*, **12**:92–97, 2016.

[123] A. W. Tsen, B. Hunt, Y. D. Kim, Z. J. Yuan, S. Jia, R. J. Cava, J. Hone, P. Kim, C. R. Dean, and A. N. Pasupathy. Nature of the quantum metal in a two-dimensional crystalline superconductor. *Nature Physics*, **12**:208–212, 2016.

[124] T. Georgiou, R. Jalil, B. D. Belle, L. Britnell, R. V. Gorbachev, S. V. Morozov, Y.-J. Kim, A. Gholinia, S. J. Haigh, O. Makarovsky, L. Eaves, L. A. Ponomarenko, A. K. Geim, K. S. Novoselov, and A. Mishchenko. Vertical field-effect transistor based on grapheneWS_2 heterostructures for flexible and transparent electronics. *Nature Nanotechnology*, **8**:100–103, 2013.

[125] N. Yabuki, R. Moriya, M. Arai, Y. Sata, S. Morikawa, S. Masubuchi, and T. Machida. Supercurrent in van der Waals Josephson junction. *Nature Communications*, **7**:10616, 2016.

[126] Y. Cao, V. Fatemi, S. Fang, K. Watanabe, T. Taniguchi, E. Kaxiras, and P. Jarillo-Herrero. Unconventional superconductivity in magic-angle graphene superlattices. *Nature*, **556**:43–50, 2018.

[127] Y. Cao, V. Fatemi, A. Demir, S. Fang, S. L. Tomarken, J. Y. Luo, J. D. Sanchez-Yamagishi, K. Watanabe, T. Taniguchi, E. Kaxiras, R. C. Ashoori, and P. Jarillo-Herrero. Correlated insulator behaviour at half-filling in magic-angle graphene superlattices. *Nature*, **556**:80–84, 2018.

[128] T. Kiss, T. Yokoya, A. Chainani, S. Shin, T. Hanaguri, M. Nohara, and H. Takagi. Charge-order-maximized momentum-dependent superconductivity. *Nature Physics*, **3**:720–725, 2007.

[129] T. Yokoya, T. Kiss, A. Chainani, S. Shin, M. Nohara, and H. Takagi. Fermi Surface Sheet-Dependent Superconductivity in 2H-NbSe2. *Science*, **294**(5551):2518–2520, 2001.

[130] D. J. Rahn, S. Hellmann, M. Kalläne, C. Sohrt, T. K. Kim, L. Kipp, and K. Rossnagel. Gaps and kinks in the electronic structure of the superconductor 2H-$NbSe_2$ from angle-resolved photoemission at 1 K. *Phys. Rev. B*, **85**:224532, Jun 2012.

[131] D. E. Moncton, J. D. Axe, and F. J. DiSalvo. Study of Superlattice Formation in 2H-$NbSe_2$ and 2H-$TaSe_2$ by Neutron Scattering. *Phys. Rev. Lett.*, **34**:734–737, Mar 1975.

[132] M. Barmatz, L. R. Testardi, and F. J. Di Salvo. Elasticity measurements in the layered dichalcogenides $TaSe_2$ and $NbSe_2$. *Phys. Rev. B*, **12**:4367–4376, Nov 1975.

[133] Matteo Calandra, I. I. Mazin, and Francesco Mauri. Effect of dimensionality on the charge-density wave in few-layer 2H-$NbSe_2$. *Phys. Rev. B*, **80**:241108, Dec 2009.

[134] D J Eaglesham, S McKernan, and J W Steeds. A double honeycomb of discommensurations in the triply-incommensurate state of 2H-$NbSe_2$. *Journal of Physics C: Solid State Physics*, **18**(1):L27–L30, jan 1985.

[135] A.V. Skripov and A.P. Stepanov. NMR study of the phasing of charge density waves in 2H-$NbSe_2$. *Solid State Communications*, **53**(5):469 – 472, 1985.

[136] C Berthier. NMR study on a 2H-$NbSe_2$ single crystal: A microscopic investigation of the charge density waves state. *Journal of Physics C: Solid State Physics*, **11**(4):797–814, feb 1978.

[137] Gyeongcheol Gye, Eunseok Oh, and Han Woong Yeom. Topological Landscape of Competing Charge Density Waves in 2H-$NbSe_2$. *Phys. Rev. Lett.*, **122**:016403, Jan 2019.

[138] Anjan Soumyanarayanan, Michael M. Yee, Yang He, Jasper van Wezel, Dirk J. Rahn, Kai Rossnagel, E. W. Hudson, Michael R. Norman, and Jennifer E. Hoffman. Quantum phase transition from triangular to stripe charge order in $NbSe_2$. *Proceedings of the National Academy of Sciences*, **110**(5):1623–1627, 2013.

[139] F. Flicker and J. van Wezel. Charge order from orbital-dependent coupling evidenced by $NbSe_2$. *Nature Communications*, **6**:7034, 2015.

[140] N. Tsuda, K. Nasu, A. Fujimori, and K. Siratori. *Electronic Conduction in Oxides,* Springer Series in Solid State Sci. Vol. 94. Springer-Verlag Berlin Heidelberg, 1991.

[141] R. Sooryakumar and M. V. Klein. Raman Scattering by Superconducting-Gap Excitations and Their Coupling to Charge-Density Waves. *Phys. Rev. Lett.*, **45**:660–662, Aug 1980.

[142] R. Sooryakumar and M. V. Klein. Raman scattering from superconducting gap excitations in the presence of a magnetic field. *Phys. Rev. B*, **23**:3213–3221, Apr 1981.

[143] P. B. Littlewood and C. M. Varma. Gauge-Invariant Theory of the Dynamical Interaction of Charge Density Waves and Superconductivity. *Phys. Rev. Lett.*, **47**:811–814, Sep 1981.

[144] P. B. Littlewood and C. M. Varma. Amplitude collective modes in superconductors and their coupling to charge-density waves. *Phys. Rev. B*, **26**:4883–4893, Nov 1982.

[145] T. Cea and L. Benfatto. Nature and Raman signatures of the Higgs amplitude mode in the coexisting superconducting and charge-density-wave state. *Phys. Rev. B*, **90**:224515, Dec 2014.

[146] Romain Grasset, Tommaso Cea, Yann Gallais, Maximilien Cazayous, Alain Sacuto, Laurent Cario, Lara Benfatto, and Marie-Aude Méasson. Higgs-mode radiance and charge-density-wave order in 2H-$NbSe_2$. *Phys. Rev. B*, **97**:094502, Mar 2018.

[147] M.-A. Méasson, Y. Gallais, M. Cazayous, B. Clair, P. Rodière, L. Cario, and A. Sacuto. Amplitude Higgs mode in the $2H-NbSe_2$ superconductor. *Phys. Rev. B*, **89**:060503, Feb 2014.

[148] K. S. Novoselov, A. Mishchenko, A. Carvalho, and A. H. Castro Neto. 2D materials and van der Waals heterostructures. *Science*, **353**(6298), 2016.

[149] H. Kambara, T. Matsui, Y. Niimi, and Hiroshi Fukuyama. Construction of a versatile ultralow temperature scanning tunneling microscope. *Review of Scientific Instruments*, **78**(7):073703, 2007.

[150] C. Kittel. *Introduction to Solid State Physics: 8th ed.* Wiley, New York, 2016.

[151] E. M. Standifer, D. H. Jundt, R. G. Norwood, and P. F. Bordui. Chemically reduced lithium niobate single crystals: processing, properties and improvements in SAW device fabrication and performance. In *Proceedings of the 1998 IEEE International Frequency Control Symposium (Cat. No.98CH36165)*, pages 470–472, May 1998.

[152] I. Tamir, A. Benyamini, E. J. Telford, F. Gorniaczyk, A. Doron, T. Levinson, D. Wang, F. Gay, B. Sacépé, J. Hone, K. Watanabe, T. Taniguchi, C. R. Dean, A. N. Pasupathy, and D. Shahar. Sensitivity of the superconducting state in thin films. *Science Advances*, **5**(3), 2019.

[153] M. K. Ekström, T. Aref, J. Runeson, J. Björck, I. Boström, and P. Delsing. Surface acoustic wave unidirectional transducers for quantum applications. *Applied Physics Letters*, **110**(7):073105, 2017.

[154] S. Bhattacharya and M. J. Higgins. Dynamics of a disordered flux line lattice. *Phys. Rev. Lett.*, **70**:2617–2620, Apr 1993.

[155] R. D. Merithew, M. W. Rabin, M. B. Weissman, M. J. Higgins, and S. Bhattacharya. Persistent Metastable States in Vortex Flow at the Peak Effect in $NbSe_2$. *Phys. Rev. Lett.*, **77**:3197–3199, Oct 1996.

[156] T. C. Padmore and G. I. Stegeman. Nonlinear interaction between oppositely propagating surface waves. *Applied Physics Letters*, **27**(1):3–5, 1975.

[157] D. H. McMahon. Acoustic Second- Harmonic Generation in Piezoelectric Crystals. *The Journal of the Acoustical Society of America*, **44**(4):1007–1013, 1968.

[158] J. Nagel, D. Speer, T. Gaber, A. Sterck, R. Eichhorn, P. Reimann, K. Ilin, M. Siegel, D. Koelle, and R. Kleiner. Observation of Negative Absolute Resistance in a Josephson Junction. *Phys. Rev. Lett.*, **100**:217001, May 2008.

[159] Takashi Oka and Sota Kitamura. Floquet Engineering of Quantum Materials. *Annual Review of Condensed Matter Physics*, **10**(1):387–408, 2019.

[160] J. Yi and Sung-Ik Lee. Quantum description of a Josephson junction coupled to a charge-density wave. *Phys. Rev. B*, **62**:9892–9895, Oct 2000.

[161] R. Duhot, S.and Mélin. Dephasing of Andreev pairs entering a charge density wave. *The European Physical Journal B*, 55(3):289–296, Feb 2007.

[162] M. I. Visscher and B. Rejaei. Josephson Current through Charge Density Waves. *Phys. Rev. Lett.*, **79**:4461–4464, Dec 1997.

[163] S. Tran, J. Sell, and J. R. Williams. Dynamical Josephson effects in $NbSe_2$. arXiv:1903.00453 [cond-mat.supr-con], Mar 2019.

[164] S. H. Strogatz. *Nonlinear Dynamics and Chaos: With Applications to Physics, Biology, Chemistry, and Engineering*. Westview Press, Cambridge, MA, 1994.

[165] Yongchang Ma, Yanhui Hou, Cuimin Lu, Lijun Li, and Cedomir Petrovic. Possible origin of nonlinear conductivity and large dielectric constant in the commensurate charge-density-wave phase of 1T-TaS_2. *Phys. Rev. B*, **97**:195117, May 2018.

[166] S. V. Borisenko, A. A. Kordyuk, V. B. Zabolotnyy, D. S. Inosov, D. Evtushinsky, B. Büchner, A. N. Yaresko, A. Varykhalov, R. Follath, W. Eberhardt, L. Patthey, and H. Berger. Two Energy Gaps and Fermi-Surface "Arcs" in $NbSe_2$. *Phys. Rev. Lett.*, **102**:166402, Apr 2009.

[167] Kazushige Machida. Charge Density Wave and Superconductivity in Anisotropic Materials. *Journal of the Physical Society of Japan*, 53(2):712–720, 1984.

Acknowledgements

本研究は、多くの方の支えのもとに進めることができました。皆さまのご協力がなければ、本研究の成果は得られなかったと思います。

新見康洋准教授には、本研究を全面的にサポートして頂きました。ご多忙な中、突飛な発想から生まれたテーマに最後まで興味を持って議論して頂いたこと、大変感謝しております。また多くの研究者との議論の中でアイデアを生み出す姿勢は、今後の私にとっても良い指針になると思います。

小林研介教授には、当研究室で 6 年間もお世話になりました。研究の歴史的背景や動向を踏まえたご指導は教育的でした。本研究でもこれらを踏まえたご意見を頂き、研究の意義を客観的に捉える力を身につけられたと思います。

福山寛教授 (東大) には $NbSe_2$ バルク結晶を提供していただきました。また負性抵抗の実験結果について、実験的に起こり得る可能性など、ご経験に基づく的確なご指摘を頂き、結果への理解が深まりました。

青山和司助教には本研究を理論的にサポートしていただきました。理論的な取り扱いが難しい実験結果でしたが、理論モデル構築や数値計算などで何度も議論させて頂きました。青山先生との議論が無ければ、本研究の解釈には至らなかったと思います。

荒川智紀助教からは微細加工や電気測定など様々な実験技術をご教示頂

きました。また、新しい現象を観測するために実験技術を開拓し続ける姿から、研究者として重要な資質を学ばせて頂きました。

夛田博一教授 (阪大基礎工)、浜屋宏平教授 (阪大基礎工) には電子線描画装置の使用および維持管理においてお世話になりました。

佐々木潤子さん、高尾明子さんには事務の仕事でお世話になりました。また、研究室の環境面でもサポートして頂き感謝いたします。

大阪大学博士課程教育リーディングプログラム「インタラクティブ物質科学カデットプログラム」と日本学術振興会には私の博士課程を資金的にサポートして頂きました。またカデットプログラムには、長期間のインターンシップなど得難い経験の場を与えて頂きました。

山口浩司先生、畑中大樹博士をはじめとする、NTT 基礎研究所ナノメカニクス研究グループの皆さまには約 3 か月間インターンシップでお世話になりました。インターンシップを通して得た MEMS や非線形現象への理解なしでは、この博士論文は完成しなかったと思います。また、大学とは少し違った環境で研究活動に取り組めたことは、私にとっての大きな財産です。

Christopher Bäuerle 博士、Jun Liang Wang さんをはじめとする、Néel 研究所 (仏) の皆さまには約 3 か月間インターンシップでお世話になりました。単一電子輸送という大きな目標に向けて、グループが一丸となって研究に取り組む環境は私にとっては非常に新鮮でした。また Bäuerle 博士には本研究の実験技術について的確な意見を頂きました。

本研究や私の博士課程に関わって頂いた小林研究室の学生の皆さまにも感謝申し上げます。特に共同研究者である河村智哉君、藤原聖士君には、本研究の実験をサポートしていただきました。河村君には本研究以前に $NbSe_2$ を扱った実験をしており、その技術を基に本研究の技術開発を行いました。

藤原聖士君には本研究を補足する実験を手伝って貰うと同時に、今後の実験を引き継いで貰っています。これからも頑張ってください。則元将太博士 (現 OIST)、岩切秀一君、藤原浩司君とは高周波チームとして、測定系の立ち上げや技術開発などを行いました。則元博士はモノづくりの知識が豊富で、実験の質問をするといつも懇切丁寧に教えて頂きました。岩切君からは、研究やそれ以外でも独特な切り口の意見を貰えるので、いつも興味深く聞いていました。藤原浩司君には、テンポよく CDW の研究を進めてもらっており、今後の展開が楽しみです。皆さまと研究を進められたことを大変うれしく思います。

最後に、長い間、私の学生生活を支えて頂いた家族に感謝いたします。